Archives of Civil and Mechanical Engineering (2022) 22:193
https://doi.org/10.1007/s43452-022-00513-6

ORIGINAL ARTICLE

Effect of zirconium doping on the mechanical properties of $W_{1-x}Zr_xB_2$ on the basis of first-principles calculations and magnetron sputtered films

Marcin Maździarz[1] · Rafał Psiuk[1] · Agnieszka Krawczyńska[2] · Małgorzata Lewandowska[2] · Tomasz Mościcki[1]

Received: 25 March 2022 / Revised: 7 August 2022 / Accepted: 11 August 2022

Abstract
Potentially superhard $W_{1-x}Zr_xB_2$ polymorphs, hP6-P6$_3$/mmc-WB$_2$ and hP3-P6/mmm-WB$_2$, were thoroughly analyzed with zirconium doping in the range of x=0-25%, within the framework of the first-principles density functional theory, from both a structural and a mechanical point of view. The obtained results were subsequently compared with the properties of material deposited by the magnetron sputtering method. All predicted structures are mechanically and thermodynamically stable. Theoretical calculations suggest a decrease in hardness H_v and fracture toughness K_{IC} of the hP6 phase with zirconium doping but no such effect on the hP3 phase. It was observed that an additional defect in the analyzed structure significantly weakens the hP6 phase but strengthens the hP3 phase. The deposited films are characterized by greater hardness but lower fracture toughness. The results of experiments show that not only is solid solution hardening responsible for strengthening the predicted new material but also the change in microstructure, the *Hall–Petch* effect and vacancies.

Keywords Ab initio · Transition metal borides · Mechanical properties · Magnetron sputtered coatings · Hardness

1 Introduction

The need to discover new materials is a scientific and industrial topic covering many different applications. Recent studies on superhard materials have shown that computational-based understanding and modeling serves as a reliable trend indicator which can be used to experimentally design new materials and their special properties [1]. Transition metal borides are an extremely promising but, so far, poorly researched class of materials that can be used in a wide variety of applications, from wear resistant tools [2] to nuclear fusion equipment [3]. Unlike nitrides or carbides, the knowledge regarding these materials is not very large and requires further research, especially into compounds like ternary borides with improved ductility and increased crack resistance, correlated with great hardness. Although there are experimental and theoretical studies on binary borides [4], a tungsten diboride doped with transition metals has been poorly explored.

Particularly noteworthy are tungsten borides doped by transition metals. Recent experimental studies show that the introduction of tantalum [5] or zirconium [6] into the WB_2 crystal lattice can provide an opportunity to create a new group of hard and refractory materials. Theoretical and experimental studies have mainly been concerned with obtaining this material in the form of coatings. In the case of alloying with tantalum, experimental studies have shown that layers obtained by magnetron sputtering are characterized by great hardness (approximately 45 GPa) and fracture toughness K_{IC} values of 3.0 MPa$\sqrt{m}$, which make this compound much better than common TiN, $Ti-Si-N$, and $(Ti, Al)N$

✉ Marcin Maździarz
mmazdz@ippt.pan.pl

Rafał Psiuk
rpsiuk@ippt.pan.pl

Agnieszka Krawczyńska
agnieszka.krawczynska@pw.edu.pl

Małgorzata Lewandowska
malgorzata.lewandowska@pw.edu.pl

Tomasz Mościcki
tmosc@ippt.pan.pl

[1] Institute of Fundamental Technological Research Polish Academy of Sciences, Pawińskiego 5B, Warsaw 02-106, Poland

[2] Faculty of Materials Science and Engineering, Warsaw University of Technology, Wołoska 141, Warsaw 02-507, Poland

Published online: 30 August 2022

[5]. Similarly, $W_{0.8}Zr_{0.2}B_{1.9}$ coatings deposited by RF magnetron sputtering are superhard ($H_v = 43.9 \pm 3.3$ GPa) and possess a fracture toughness $K_{IC} = 1.77$ MPa$\sqrt{m}$ [7]. Psiuk et al. [6] proposed a combined magnetron sputtering and pulsed laser deposition technique for doping WB_2 films by zirconium. Film obtained with a fluence of 1.06 J/cm^2 ($\sim 2\%$ *Zr* at.) showed ductile–brittle behavior and was superhard $H_v = 40 \pm 4$ GPa, incompressible $R_s = 12 \pm 1$ GPa, and possessed a relatively low Young's modulus $E = 330 \pm 32$ GPa and high elastic recovery $W_e = 0.9$ [6]. Additionally, when alloyed with *Ta* [8] or *Zr* [9] WB_2 coatings are stable, even at 700 °C. Experimental studies also showed that, for different transition metals (*Ta* or *Zr*) and tungsten contents, thin magnetron-deposited films of $W_{1-x}Ta_xB_{2-z}$ crystallize similarly to WB_{2-z} mainly in terms of its α type structure (space group 191-P6/mmm) [10]. By means of density functional theory (DFT) calculations, the α-structure of WB_2 is metastable and was classified as a ductile material [10]. It should be noted that α-WB_2 is characterized by relatively low hardness ($H_v = 10$ GPa) [11]. Other studies on diborides showed that WB_x also preferred to crystallize in other hexagonal structures, i.e. W_2B_{5-x}-based structure (ω, space group 194-P6$_3$/mmc) [10]. A characteristic for the AlB_2 structure type is the hexagonal shaped unit cell with alternating stacking of covalent bonded boron hexagons and metal layers. The W_2B_{5-x} structure also consists of a hexagonal unit cell but with alternating flat and puckered boron layers between the metal layers [12]. Such a structure changes the properties to brittle but hard ($H_v = 39$ GPa [13]), which is closer to experimental values. In connection with such differences, an explanation of this phenomenon has been undertaken. Using DFT *ab initio* methods, it has been shown that vacancies can be responsible for metastable α stabilization in a ternary system [14]. The results presented by Fuger et al. [14] indicated that α-WB_{2-x} stabilized by *B* vacancies possesses hardness comparable to a thermodynamically favorable ω-WB_2. However, there is anisotropy in the elastoplastic behavior of α-WB_{2-x} stabilized by boron vacancies. The maximal hardness was determined for (0001) oriented films, linearly decreasing by more than 15 GPa with an increasing $(10\bar{1}1)$ orientation [14]. Another problem is that, by removing boron atoms, the stoichiometry and space group of the WB_2 compound is changed. It is known that W_2B_3 ($WB_{1.5}$) is harder than hP3-P6/mmm-WB_2, see [11]. Unfortunately, the influence of defects on the hardness of materials is inconclusive. For example, the microhardness of *FeAl* increases with the square root of the vacancy concentration [15]. The vacancies change the mechanical properties of $\alpha - Zr$ and increase the hardness of the crystal [16] but in the case of CrB_4 compound the hardness is reduced [17]. However, alloying elements can also increase mechanical properties, as well as vacancies. Fuger et al. [5] proved theoretically and experimentally that alloying with tantalum with a content below 30% at. can increase hardness with increasing *Ta* content, due to solid solution hardening effects. In the case of zirconium, theoretical studies were only presented for $Zr_xW_{1-x}B_2$ with a zirconium content of $x > 0.24$ [18]. In this work, Gu et al. reported a systematic first-principles study of a large series of group-IVB, VB and VIB dual-TM diborides with a hexagonal structure, to explore the brittle-ductile relation. For the $W_{0.75}Zr_{0.25}B_2$ compound, the starting structure was hexagonal ZrB_2 in P6/mmm symmetry, which is the hardest form of a stable polymorph of zirconium diboride [19]. The replacement of six of the eight zirconium atoms with tungsten resulted in a significant decrease in hardness ($H_v = 17.44$ GPa). At the same time, this compound is characterized by a relatively high Poison's ratio ($\nu = 0.268$) and a high Pugh's ratio ($B/G = 1.825$) (the ratio of bulk and shear modulus), which qualifies it as a ductile material [18].

As has been mentioned, doping WB_2 with small amounts of zirconium improves the properties of the deposited coatings, similar to tantalum. Due to the fact that there are no theoretical structural calculations in this case, this work undertook to determine the WB_2 structures doped with zirconium ($W_{1-x}Zr_xB_2$ where $x = 0$–0.24). A comparative experiment will try to explain possible mechanisms for the hardening of magnetron sputtered $W - Zr - B$ coatings, which can then be used successfully in current engineering projects.

2 Methodology

2.1 Computational methodology

2.1.1 Ab Initio calculations

First-principles calculations, based on density functional theory (DFT) [20, 21] within the pseudopotential plane-wave approximation (PP-PW) implemented in ABINIT [22, 23] software, were carried out in this study. Projector augmented-wave formulation (PAW) pseudopotentials [24] were employed to represent the interactions of the ionic core and non-valence electrons.

The effect of an exchange-correlation (XC) functional on calculated lattice constants in WB_x structures was analyzed in [13]. Analysis of the experimental data [25] suggests that it is reasonable to use a local density approximation (LDA) [26, 27] as an XC functional. The projector augmented wave method (PAW) pseudopotentials used for LDA XC functionals were obtained from the PseudoDojo project [28]. The following valence electron configurations were used: $5s^25p^65d^46s^2$ for *W*, $2s^22p^1$ for *B* and $4d^25s^2$ for *Zr*, respectively.

The calculation accuracy settings correspond to those in the work by [19].

2.1.2 Generation and optimization of structures

Tungsten borides crystallize in various phases and WB_2 hP6-$P6_3/mmc$ (Fig. 1a) seems to be the hardest one but it has not yet been synthesized. WB_2 hP3-P6/mmm (191) (Fig. 1b) and WB_2 hP12-P6/mmm (191) have been manufactured and examined experimentally [11, 13] but hP3 dominates in our experimental samples. How the addition of zirconium affects the mechanical properties of WB_2 hP6-$P6_3/mmc$ (194) phase (Fig. 1a) and WB_2 hP3-P6/mmm (191) phase (Fig. 1b) was investigated.

In order to do this, the following supercells of WB_2-hP6 were generated: $2 \times 1 \times 1$ (12 atoms), $3 \times 1 \times 1$ (18 atoms), $2 \times 2 \times 1$ (24 atoms), $3 \times 2 \times 1$ (36 atoms), $2 \times 2 \times 2$ (48 atoms), $3 \times 3 \times 1$ (54 atoms), $3 \times 2 \times 2$ (72 atoms), $4 \times 4 \times 1$ (96 atoms) and $2 \times 2 \times 1$ defected with WB_2 cluster ($24 - 3 = 21$ atoms). For WB_2-hP3, the supercells were: $2 \times 2 \times 1$ (12 atoms), $2 \times 2 \times 2$ (24 atoms), $3 \times 3 \times 1$ (27 atoms), $3 \times 2 \times 2$ (36 atoms), $3 \times 3 \times 2$ (54 atoms), $3 \times 3 \times 3$ (81 atoms) and $2 \times 2 \times 2$ defected with WB_2 cluster ($24 - 3 = 21$ atoms); one arbitrary tungsten atom was replaced with a zirconium atom. In the two structures with defects, a cluster of three atoms was removed, i.e. a triple defect consisting of a *W* atom and two *B* atoms; such a defect does not disturb the chemical composition of the metal and the boron. It was observed in [16] that a cluster of defects modifies the hardness of pure *Zr* more than uniformly distributed defects. Examples of the generated supercells are shown in Fig. 2a, b. It did not matter which *W* atom was replaced by *Zr* because they are equivalent. However, the doped structure has a different symmetry than the symmetry of the original WB_2, see Table 1. The generated structures were then fully optimized, in terms of cell geometry and atomic coordinates, as in [19].

2.1.3 Formation enthalpy and cohesive energy

The formation enthalpy and cohesive energy of $W_{1-x}Zr_xB_2$ structures were determined as follows [29, 30]:

$$\triangle_f H(W_{1-x}Zr_xB_2) = E_{\mathrm{coh}}(W_{1-x}Zr_xB_2) - (1-x)E_{\mathrm{coh}}(W) - xE_{\mathrm{coh}}(Zr) - 2E_{\mathrm{coh}}(B), \quad (1)$$

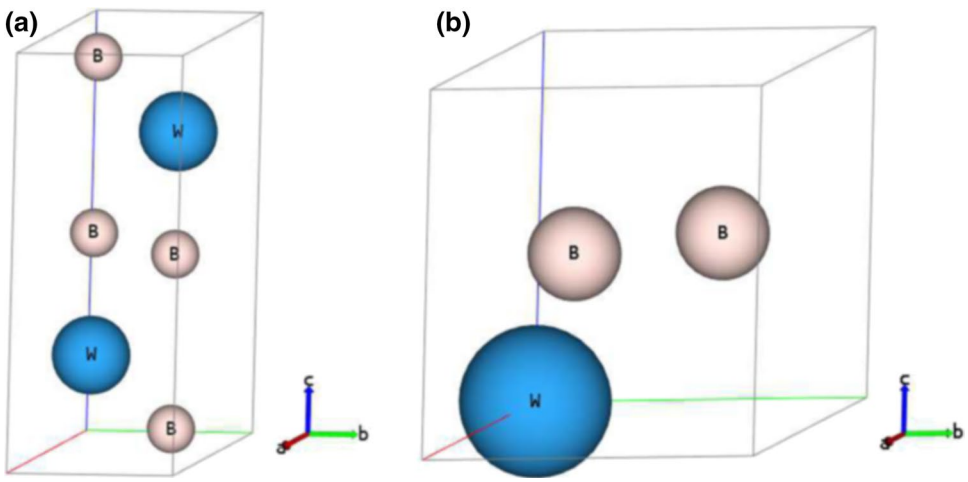

Fig. 1 Basic WB_2 cell: **a** hP6-$P6_3/mmc$ (194), **b** hP3-P6/mmm (191)

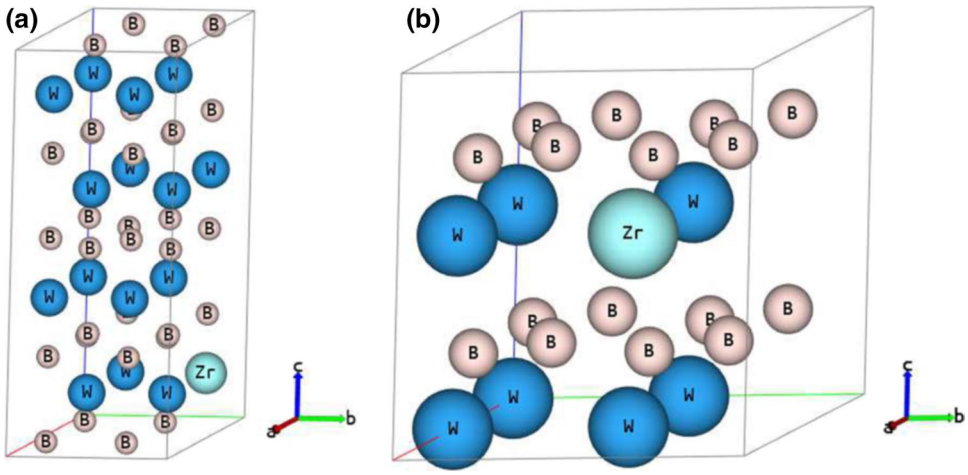

Fig. 2 $2 \times 2 \times 2$ supercell with one *W* atom replaced by a *Zr* atom: **a** $W_{0.94}Zr_{0.06}B_2$ ($W_{15/16}Zr_{1/16}B_2$), **b** $W_{0.875}Zr_{0.125}B_2$ ($W_{7/8}Zr_{1/8}B_2$)

Table 1 Chemical formula; Space group; Pearson symbol; proportion of *Zr* dopant: $Zr/(W+Zr)$; Volume per atom (Å/Atom); formation enthalpy $\triangle_f H$ (eV/Atom); cohesive energy E_c (eV/Atom) (open markers refer to structures with a defect)

Sample	Space group	Pearson symbol	$\frac{Zr}{W+Zr}$	Vol/atom	$-\triangle_f H$	$-E_c$
hP6						
WB_2	$P6_3/mmc$ (194)	hP6	0/1	9.298	0.495	8.880
$W_{0.75}Zr_{0.25}B_2$	Pmm2 (25)	oP12	1/4	9.775	0.395	8.300
$W_{0.835}Zr_{0.165}B_2$	Pm (6)	mP18	1/6	9.615	0.423	8.488
$W_{0.875}Zr_{0.125}B_2$	Amm2 (38)	oC24	1/8	9.533	0.438	8.583
$W_{0.915}Zr_{0.085}B_2$	Pm (6)	mP36	1/12	9.455	0.455	8.681
$W_{0.937}Zr_{0.063}B_2$	Amm2 (38)	oC48	1/16	9.417	0.466	8.731
$W_{0.944}Zr_{0.056}B_2$	Amm2 (38)	oC54	1/18	9.403	0.468	8.747
$W_{0.958}Zr_{0.042}B_2$	Pm (6)	mP72	1/24	9.381	0.475	8.780
$W_{0.969}Zr_{0.031}B_2$	Amm2 (38)	oC96	1/32	9.360	0.479	8.805
$W_{0.857}Zr_{0.143}B_2$ °	P1 (1)	aP21	1/7	10.729	0.166	8.277
hP3						
WB_2	P6/mmm (191)	hP3	0/1	8.918	0.299	8.685
$W_{0.75}Zr_{0.25}B_2$	P6/mmm (191)	hP12	1/4	8.885	0.678	8.408
$W_{0.875}Zr_{0.125}B_2$	P6/mmm (191)	hP24	1/8	8.762	0.438	8.583
$W_{0.889}Zr_{0.111}B_2$	P6/mmm (191)	hP27	1/9	8.738	0.391	8.563
$W_{0.915}Zr_{0.085}B_2$	P2/m (10)	mP36	1/12	8.690	0.369	8.594
$W_{0.944}Zr_{0.056}B_2$	P6/mmm (191)	hP54	1/18	8.687	0.340	8.619
$W_{0.963}Zr_{0.037}B_2$	P6/mmm (191)	hP81	1/27	8.677	0.329	8.644
$W_{0.857}Zr_{0.143}B_2$ △	P1 (1)	aP21	1/7	9.479	0.425	8.536
W	Fm-3m (225)	cF4		15.78		12.64
Zr	$P6_3/mmc$ (194)	hP2		22.30		6.87
B	R-3m (166)	hR12		20.95		6.26

$$E_{\text{coh}}(W_{1-x}Zr_xB_2) = E_{\text{total}}(W_{1-x}Zr_xB_2) - (1-x)E_{\text{iso}}(W) - xE_{\text{iso}}(Zr) - 2E_{\text{iso}}(B), \quad (2)$$

where $\triangle_f H(W_{1-x}Zr_xB_2)$ is the formation enthalpy of the $W_{1-x}Zr_xB_2$; $E_{\text{coh}}(W_{1-x}Zr_xB_2)$ is the cohesive energy of the $W_{1-x}Zr_xB_2$; $E_{\text{coh}}(W)$ is the cohesive energy of W; $E_{\text{coh}}(Zr)$ is the cohesive energy of Zr; $E_{\text{coh}}(B)$ is the cohesive energy of B; $E_{\text{tot}}(W_{1-x}Zr_xB_2)$ is the total energy of the $W_{1-x}Zr_xB_2$; $E_{\text{iso}}(W)$ is the total energy of a W atom, $E_{\text{iso}}(Zr)$ is the total energy of a Zr atom and $E_{\text{iso}}(B)$ is the total energy of a B atom.

To calculate the cohesive energy, the following reference structures were chosen: for tungsten (cF4-Fm-3m (225)), for zirconium (hP2-P6/mmc (194)) and for boron (hR12-R-3m (166)).

2.1.4 Mechanical properties calculations

The theoretical ground state elastic constants C_{ij} of all analyzed structures were calculated using the metric tensor formulation of strain in density functional perturbation theory (DFPT) [31]. Isotropised bulk modulus $\boldsymbol{B}$, shear modulus $\boldsymbol{G}$, Young's modulus $\boldsymbol{E}$ and Poisson's ratio ν were estimated using a Voigt–Reuss–Hill average [32, 33].

In order to verify the mechanical stability of all the structures, positive definiteness of the stiffness tensor was examined [34] by calculating Kelvin moduli, i.e. eigenvalues of stiffness tensor written in *second-rank tensor* notation [35].

Vickers hardness H_v and fracture toughness K_{IC} of all the $W_{1-x}Zr_xB_2$ samples analyzed were estimated with the use of semi-empirical formulas developed in [36].

The Pugh ratio B/G, where B is the bulk modulus and G is the shear modulus, represents the competition between the following two processes: plasticity and fracture. If plasticity is easier to achieve, then a material will tend to be ductile, whereas if fracturing is easier, then a material will tend to be brittle. Pugh [37] proposed relations between the elastic and plastic properties of pure polycrystalline metals possessing the same lattice structure. It was also shown that this criterion is correct for both cubic and hexagonal structures. Ratio B/G is affected by the crystal structure; however, these are usually neglected, to enable easy comparison of materials. The basic form of this criterion is as follows:

$$P_u \approx \frac{c\mathbf{B}a}{\mathbf{G}b}, \quad (3)$$

where b is the Burgers vector, c is a constant for a particular crystal structure and a is a lattice parameter. The effects of crystal structure can be neglected if b/ac is constant in an investigated group of materials. Hence the ratio B/G provides a measure of the likely nature of a material's failure

as follows: a low value of B/G implies brittle failure, while a high value implies ductile failure. This assumes that the changes in crystal structure affect both processes to the same degree. In the case of boride films, this assumption was checked in [10]. Obtained results for the Pugh ratio were compared with two other theories: the Frantsevich criterion (regarding Poisson's ratio) and the Cauchy pressure ($C_{12} - C_{44}$)— Pettifor criterion. Good compliance was obtained and a ductile behavior for borides was established for $B/G < 1.75$.

Flexibility of hard nanocomposite coatings was estimated by the H_v/E^* ratio, where $E^* = E/(1-\nu^2)$ [38].

2.2 Experimental methods

2.2.1 Process of magnetron sputtering

The ternary sputtering targets were produced with a diameter of 25.4 mm, through the Spark Plasma Sputtering (SPS) process from boron (purity: 96.8%, average particle size APS: 1 µm, Sigma Aldrich), tungsten (purity: 99.9%, APS: 25 µm, Sigma Aldrich), and zirconium (purity: 99.8%, APS: 250-350 µm, Sigma Aldrich). The composition used for deposition targets was $WB_{2.5}$, $W_{0.92}Zr_{0.08}B_{2.5}$, $W_{0.84}Zr_{0.16}B_{2.5}$, $W_{0.76}Zr_{0.24}B_{2.5}$. Detailed information on the SPS targets are presented in [39].

The target was mounted in a water-cooled 1-inch magnetron sputtering cathode (Kurt J. Lesker). The deposition process occurred in a vacuum chamber, initially pumped to 2×10^{-5} mbar and then filled with argon to a working pressure of 9×10^{-3} mbar. The gas flow of argon was 19 mL/min. Prior to each deposition, the target was sputtered for 5 min, in order to ensure its clean surface and stable sputtering conditions. During all of the experiments, the power supplied to the magnetron cathode was maintained at 50 W. Films were deposited for 180 min on *Si* (100) (Institute of Electronic Materials Technology, Poland) and nitrided QRO90 steel substrates were heated up to 500 °C and positioned 40 mm in front of the target. The deposited coatings were approximately 2.8 µm thick.

2.2.2 Characterization

The surface cross section and the chemical composition were investigated using a Hitachi Su8000 scanning electron microscope (SEM). The chemical composition was investigated using a JEOL JSM-6010Plus SEM equipped with an Energy Dispersive X-Ray Spectroscope (EDS). Microstructural studies were carried out on the cross sections of deposited films cut perpendicularly to the surface. Before cross sectional observations were made, the sample was cut in the middle by a precision saw. The area for observations was prepared using an IM4000 Hitachi ion milling system. Electron-transparent samples were prepared by a focus ion beam (FIB) to a thickness of ≈ 300 nm. The acceleration voltage of the beam was set to 40 kV, while the beam current was controlled with the size of aperture depending on the stage of preparation. Then, lamellas were gently thinned by a low-energy $Ar+$ ion beam system (between 0.6 and 1 keV) to a final thickness of ≈100 nm, to limit additional defects present in the microstructure, introduced by the FIB beam. General observations were made with the use of a Hitachi HD2700 scanning transmission electron microscope (STEM), operated at 200 kV. The STEM images were taken in bright-field (BF) and selective area electron diffraction (SAED) mode. In SAED mode, the patterns were acquired by inserting a 250 nm aperture. During the measurement of the chemical composition of the deposited coatings, an accelerating voltage of 5 kV was used. Moreover, the system was calibrated with the use of commercially available target W_2B_5 (purity 99.9%, Huizhou Tian Yi Rare Material Co. Ltd). The authors are aware of the uncertainties in boron measurement with EDS, which are related to the proximity of the boron and carbon peaks, as well as carbon contamination. The phase composition and crystal structure of deposited layers were characterized by an X-Ray Diffractometer (Bruker D8 Discover, $\lambda = 1.5418$ Å). Measurements were taken in 2Θ scan mode, with the source fixed at the 8° position. In this configuration, it was possible to avoid the signal from the substrate, while maintaining high intensity of the signal originating primarily from the coating.

2.2.3 Mechanical properties

Vickers hardness measurements were performed using a Wilson VH1102 microhardness tester (Buehler, Lake Bluff, IL, USA). A load of 10 g was used to measure the hardness of the deposited coatings and 10 indentations were performed on each sample. A VK-X100 laser confocal microscope (Keyence, Osaka, Japan) was used to measure the indents. The method of measurement and recalculation of microhardness due to substrate influence was earlier described in [7]. The Laugier model equation [40] was used to analyze changes in fracture toughness (K_{IC}). For each coating, based on a group of 10 indentations, the mean value of l and a crack dimensions were determined, similarly to [41]. Equation 4 was used to evaluate the fracture toughness of the deposited coatings.

$$K_{IC} = x_v \left(\frac{a}{l}\right)^{\frac{1}{2}} \left(\frac{E}{H_v}\right)^{\frac{2}{3}} \frac{P}{c^{\frac{3}{2}}}, \tag{4}$$

where K_{IC} is fracture toughness (MPa$\sqrt{m}$); x_v is the indenter geometry factor (for the Laugier Equation, $x_v = 0.016$); E-Young modulus of coating (GPa) (values were taken from [9]); H_v is the Vickers hardness of the coating (GPa); P is the indentation load (mN); a is the length from the centre of

the indent to the corner of the indent (m), l is the length of the cracks and $c = l + a$.

3 Results and discussion

3.1 DFT calculations

The resulting structures obtained from the optimization are summarized in Table 1. Crystallographic data were produced as crystallographic information files (CIFs) and their figures are attached in the Appendix.

As expected, the decrease in the proportion of *Zr* in the structures is followed by a decrease of average atomic volume, simply because the *Zr* atom is "bigger" than *W*. The opposite trend is observed for cohesive energy E_c, see Fig. 3b. The formation enthalpy $\triangle_f H$ for hP6 decreases slightly but increases significantly for hP3 as the proportion of zirconium increases, see Fig. 3a. It should be noted that there are negative values in Table 1, Fig. 3a, b. This suggests that hP6 doped structures are less thermodynamically stable than pure ones but are still stable due to the negative value of $\triangle_f H$ and, conversely, for hP3 doped structures. Similar behavior was also observed for doping with *Ti* [12], *Al*, and *V* [42].

The calculated Kelvin moduli, i.e. the eigenvalues of stiffness tensor, for all of the analyzed structures are given in Table 2. It can be seen that the values for each sample are positive. This means that all of the structures are mechanically stable.

The symmetry of a crystal determines the symmetry of its physical properties, here we are interested in the symmetry of the stiffness tensor and the number of distinct elastic constants [43]. For a hexagonal crystal system there are five distinct elastic constants; nine for orthorhombic, 13 for monoclinic and 21 for triclinic, respectively. For clarity of presentation, the full stiffness tensors for each structure are included in the Appendix. The derived quantities from the elasticity constants are listed in Table 3 and depicted in Fig. 4a, b as well as Fig. 5a, b.

An increase in the proportion of *Zr* in hP6-$W_{1-x}Zr_xB_2$ reduces the value of bulk modulus B, shear modulus G, Young's modulus E, hardness H_v and fracture toughness K_{IC}. The Poisson's ratio ν is nearly constant at about 0.2. The Pugh's ratio B/G is a relationship associated with the brittle or ductile behavior of materials. A higher B/G ratio corresponds to higher ductility [37]. In our case, the doping of *Zr* increases ductility and, at the same time, reduces the H_v/E^* ratio, i.e. it is some measure of flexibility of hard nanocomposite coatings. A triple defect in hP6 has significantly reduced bulk modulus, shear modulus, Young's modulus, hardness and fracture toughness, while it has increased B/G and the Poisson's ratio ν. For hP3-$W_{1-x}Zr_xB_2$, it is difficult to find any trend for the calculated parameters as a function of the proportion of *Zr* and it can be assumed that they are almost invariable. An exception to this is defected hP3. In this case, the shear modulus, Young's modulus and hardness increased significantly, together with a decrease in ductility. Although this was not the main focus of the present study, it seems that defects affect $W_{1-x}Zr_xB_2$ properties more strongly than *Zr* doping, see Fig. 4a, b as well as Fig. 5a, b.

3.2 Comparison with the experiment

In Fig. 6, the exemplary results of SEM investigations are shown. The surfaces of the deposited films are smooth and the cross-section is uniform, at a thickness of 2.8 µm (Fig. 6a, b).

In Table 4, the chemical composition of the deposited films is presented. The deposited films are characterized by similar stoichiometric compositions to the predicted theoretical structures: $W_{0.835}Zr_{0.165}B_2$, $W_{0.875}Zr_{0.125}B_2$ and

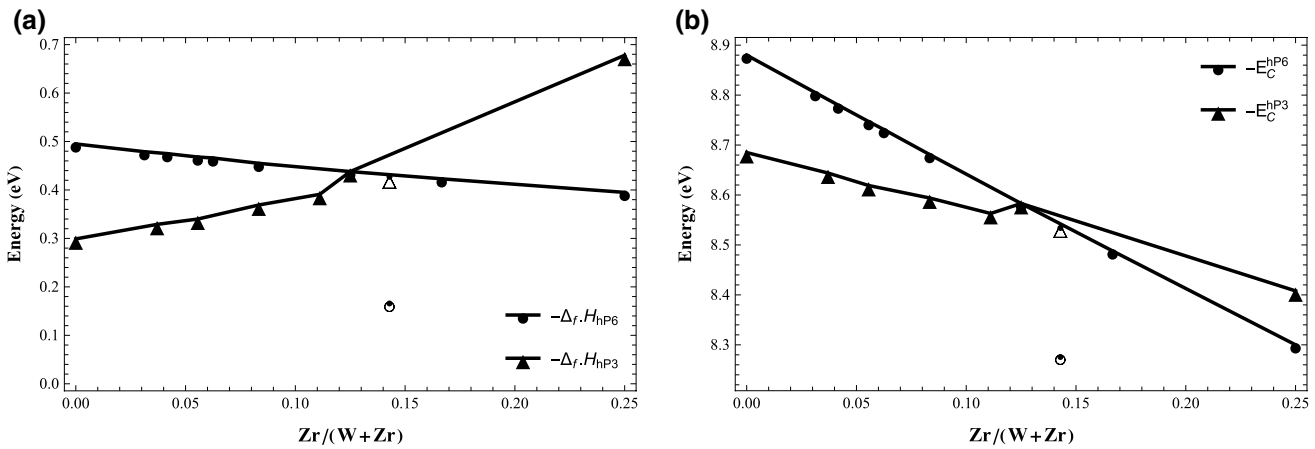

Fig. 3 $W_{1-x}Zr_xB_2$: **a** formation enthalpy $\triangle_f H$ (eV/Atom), **b** cohesive energy E_c (eV/Atom) (open markers refer to structures with a defect)

Table 2 Chemical formula; Kelvin moduli K_i (GPa) (open markers refer to structures with a defect)

Sample	K_1	K_2	K_3	K_4	K_5	K_6
hP6						
WB_2	1065.21	705.223	552.611	552.611	403.475	403.475
$W_{0.75}Zr_{0.25}B_2$	873.269	556.857	401.992	398.155	287.685	286.955
$W_{0.835}Zr_{0.165}B_2$	946.392	602.807	449.931	435.294	324.303	304.977
$W_{0.875}Zr_{0.125}B_2$	963.91	627.05	463.626	459.192	336.276	333.599
$W_{0.915}Zr_{0.085}B_2$	972.758	600.622	504.494	456.625	319.321	310.069
$W_{0.937}Zr_{0.063}B_2$	996.274	651.301	487.159	485.881	351.937	351.842
$W_{0.944}Zr_{0.056}B_2$	1025.74	652.494	504.358	503.768	358.926	350.14
$W_{0.958}Zr_{0.042}B_2$	1008.52	642.412	505.422	496.438	352.005	339.054
$W_{0.969}Zr_{0.031}B_2$	1023.54	645.426	509.716	508.957	350.915	346.937
$W_{0.857}Zr_{0.143}B_2$ °	711.34	371.68	335.199	203.228	193.159	181.8
hP3						
WB_2	1016.91	430.75	430.75	291.3	291.3	188.836
$W_{0.75}Zr_{0.25}B_2$	948.439	499.373	499.373	389.021	389.021	234.097
$W_{0.875}Zr_{0.125}B_2$	930.091	417.4	417.4	329.6	329.6	157.909
$W_{0.889}Zr_{0.111}B_2$	969.709	454.265	454.265	316.769	316.769	210.891
$W_{0.915}Zr_{0.085}B_2$	972.166	493.784	425.464	313.263	297.896	154.252
$W_{0.944}Zr_{0.056}B_2$	947.942	432.198	432.198	281.095	281.095	173.58
$W_{0.963}Zr_{0.037}B_2$	1231.2	480.557	480.557	254.257	254.257	184.116
$W_{0.857}Zr_{0.143}B_2$ △	954.279	493.506	485.974	465.791	448.814	333.79

Table 3 Chemical formula; Bulk modulus B (GPa); shear modulus G (GPa); Young's modulus E (GPa); Poisson's ratio ν; B/G Pugh's ratio; Vickers hardness H_v (GPa); hardness to modified Young's modulus ratio H_v/E^*; fracture toughness K_{IC} (MPa$\sqrt{m}$) (open markers refer to structures with a defect)

Sample	B	G	E	ν	B/G	H_v	H_v/E^*	K_{IC}
hP6								
WB_2	336.64	258.99	618.40	0.19	1.30	34.27	0.053	5.46
$W_{0.75}Zr_{0.25}B_2$	273.45	190.19	463.19	0.22	1.44	22.20	0.046	3.78
$W_{0.835}Zr_{0.165}B_2$	295.13	208.71	506.68	0.21	1.41	24.71	0.047	4.27
$W_{0.875}Zr_{0.125}B_2$	305.66	218.50	529.36	0.21	1.40	26.16	0.047	4.52
$W_{0.915}Zr_{0.085}B_2$	296.39	216.42	522.16	0.21	1.37	26.56	0.049	4.37
$W_{0.937}Zr_{0.063}B_2$	313.63	229.70	553.88	0.21	1.37	28.30	0.049	4.76
$W_{0.944}Zr_{0.056}B_2$	319.65	234.22	564.73	0.21	1.36	28.87	0.049	4.90
$W_{0.958}Zr_{0.042}B_2$	311.88	230.88	555.55	0.20	1.35	28.85	0.050	4.77
$W_{0.969}Zr_{0.031}B_2$	315.23	233.78	562.32	0.20	1.35	29.29	0.050	4.83
$W_{0.857}Zr_{0.143}B_2$ °	229.04	123.97	315.07	0.27	1.85	15.33	0.045	2.62
hP3								
WB_2	338.603	156.057	405.825	0.30	2.17	21.18	0.047	4.28
$W_{0.75}Zr_{0.25}B_2$	313.855	193.927	482.42	0.24	1.62	22.24	0.043	4.31
$W_{0.875}Zr_{0.125}B_2$	309.088	155.367	399.212	0.28	1.99	20.12	0.046	3.86
$W_{0.889}Zr_{0.111}B_2$	322.626	168.561	430.677	0.28	1.91	21.32	0.046	4.18
$W_{0.915}Zr_{0.085}B_2$	315.932	156.585	403.15	0.29	2.02	20.45	0.047	3.96
$W_{0.944}Zr_{0.056}B_2$	313.875	151.57	391.665	0.29	2.07	20.08	0.047	3.88
$W_{0.963}Zr_{0.037}B_2$	400.584	154.824	411.463	0.33	2.59	22.52	0.049	5.09
$W_{0.857}Zr_{0.143}B_2$ △	315.691	220.832	537.228	0.22	1.43	25.89	0.046	4.68

$W_{0.915}Zr_{0.085}B_2$ for 24% at., 16% at., and 8% at. of Zr in the target, respectively. However, a marked decrease in the amount of boron in the films is noteworthy. Such a phenomenon was observed in earlier studies and can be explained by the scattering of light boron atoms on the much heavier argon [44] and tungsten in the plasma plume [45]. Next, the re-sputtering of the deposited boron by heavy tungsten atoms from the coating is also possible. Oxygen is also detected in the coatings and its content grows with an increase in zirconium.

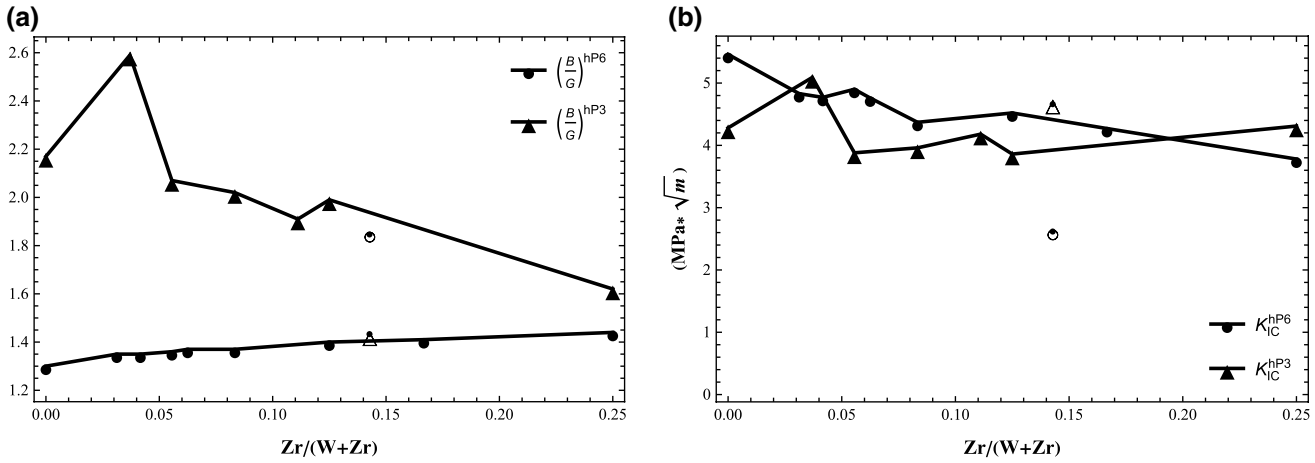

Fig. 4 $W_{1-x}Zr_xB_2$: **a** B/G Pugh's ratio, **b** fracture toughness K_{IC} (MPa$\sqrt{m}$) (open markers refer to structures with a defect)

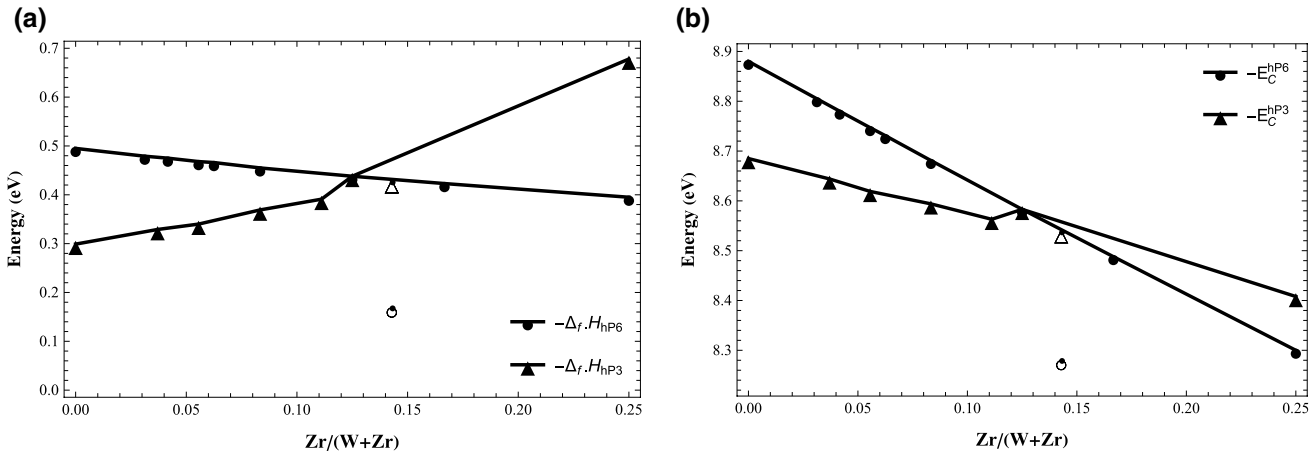

Fig. 5 $W_{1-x}Zr_xB_2$: **a** Vickers hardness H_v (GPa), **b** hardness to modified Young's modulus ratio H_v/E^* (open markers refer to structures with a defect)

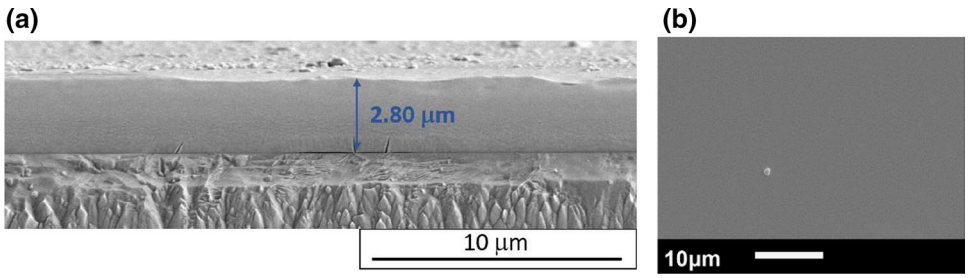

Fig. 6 SEM investigations of coating ($W_{0.84}Zr_{0.16}B_{1.52}$) deposited from target with 24% at. of zirconium on nitrided QRO90 steel substrates: **a** cross-section, **b** surface

Table 4 Chemical composition of deposited coatings

$\frac{Zr}{W+Zr}$ in target	B(% at.)	Zr(% at.)	W(% at.)	$\frac{Zr}{W+Zr}$	$\frac{B}{W+Zr}$	O(% at.)
0.00	59.4	0.0	37.3	0.00	1.59	3.3
0.08	55.2	2.9	38.0	0.07	1.35	3.8
0.16	56.7	4.6	34.7	0.12	1.44	3.9
0.24	58.0	5.9	32.1	0.16	1.52	4.0

The theoretically obtained mechanical properties are lower than those from the microhardness tests (Fig. 7a, Table 5). Taking into account the fact that the deposited coatings were approximately 2.8 µm thick, the penetration depth (Table 5) is more than 1/10 the thickness of the coatings and the influence of the substrate should be included. Therefore, the measured microhardness ($H_v^{0.01}$) was recalculated according to the method presented in [7] and compared with nanoindentation data from the literature [9]. The comparison is presented in Table 5.

Such significant differences between theoretical and experimentally measured Vickers hardness were previously observed by Fuger et al. [5, 14]. The hardness of stoichiometric-structured WB_2 (P6/mmm) was theoretically predicted as $H_v^{\text{theo}} = 21$ GPa, whereas the boron defected - $WB_{1.5}$ was 28 GPa and $H_v^{\text{theo}} = 12$ GPa for $WB_{1.8}$, respectively [14]. It is no coincidence that the experimental data where the Vickers hardness was measured by nanoindentation was $H_v^{\text{exp}} = 40.8 \pm 1.5$ GPa for single-phased α-$W_{1-x}Ta_xB_{1.87}$ coatings with $x = 0$ [5]. Large differences between theoretical and experimental values suggest that solid solution hardening is one of the strengthening mechanisms. Therefore, when new materials are theoretically designed, we should be aware of the influence of other hardening mechanisms on the mechanical properties of these materials [46].

Table 5 Vickers hardness of deposited coatings as measured, recalculated due to substrate influence and measured with nanoindentation

$\frac{Zr}{W+Zr}$ in target	Depth (µm)	$H_v^{0.01}$ (GPa)	$H_v^{0.01}$ (recalculated) (GPa)	Nanoindentation [9] (GPa)
0.00	0.53	26.9 ± 2.1	40.1 ± 3.1	45.8 ± 0.6
0.08	0.48	32.7 ± 3.4	51.3 ± 5.0	45.1 ± 1.9
0.16	0.46	34.9 ± 4.0	49.1 ± 5.0	44.3 ± 1.6
0.24	0.50	29.9 ± 2.4	43.9 ± 3.3	47.2 ± 1.6

The hardness of deposited $W_{0.84}Zr_{0.16}B_{1.52}$ sample measured under load 10 g is 29.9 ± 2.4 GPa when theoretically calculated value for $W_{0.835}Zr_{0.165}B_2$ is $H_v = 24.71$ GPa. Taking into account the measurement errors (see the error bars in Fig. 7a) for zirconium alloyed samples, the hardness value does not change substantially and average hardness is ~ 32 GPa. The lowest value was obtained for the undoped coating (26.8 GPa) whilst, in theoretical calculations, WB_2 possess a hardness of 34.3 GPa. This can be explained by the fact that tungsten borides crystallize in various phases and WB_2 hP6-P6$_3$/mmc (194) seems to be the hardest one [13]. Earlier studies have shown that the dominant phase in the deposited coatings is a much softer phase hP3-P6/mmm (191). The addition of zirconium causes rebuilding of the crystal structure and, as a consequence, changes the mechanical properties. The increase in zirconium content results in the growth of fracture toughness K_{IC} (Fig. 7b) and, for $W_{0.84}Zr_{0.16}B_{1.52}$, the differences are the lowest and K_{IC} is 3.86 ± 0.15 MPa$\sqrt{m}$; in theory, it should be 4.27 MPa$\sqrt{m}$.

A simultaneous increase of ductility and hardness is quite unusual. Such a relation was reported by Musil [38] for films with a T-structure (Thorton model). However, Musil [38] gave additional conditions for flexible hard nanocomposite coatings. Deposited films should exhibit high values of hardness and effective Young's modulus E^* ratio$H_v/E^* > 0.1$, elastic recovery $W_e > 60\%$, and compressive macrostress $\sigma < 0$. The films with a dense, void-free microstructure, composed of fibrous grains embedded in an amorphous intergrain phase, can meet these assumptions. Such a structure can be roughly compared to multi-layered coatings with a layer thickness of about 10 nm. In such a case, coherency stresses and misfit dislocation arrays, elastic mismatches between the layer materials, and the change of the bonding characteristics with decreasing layer thicknesses can be responsible for the

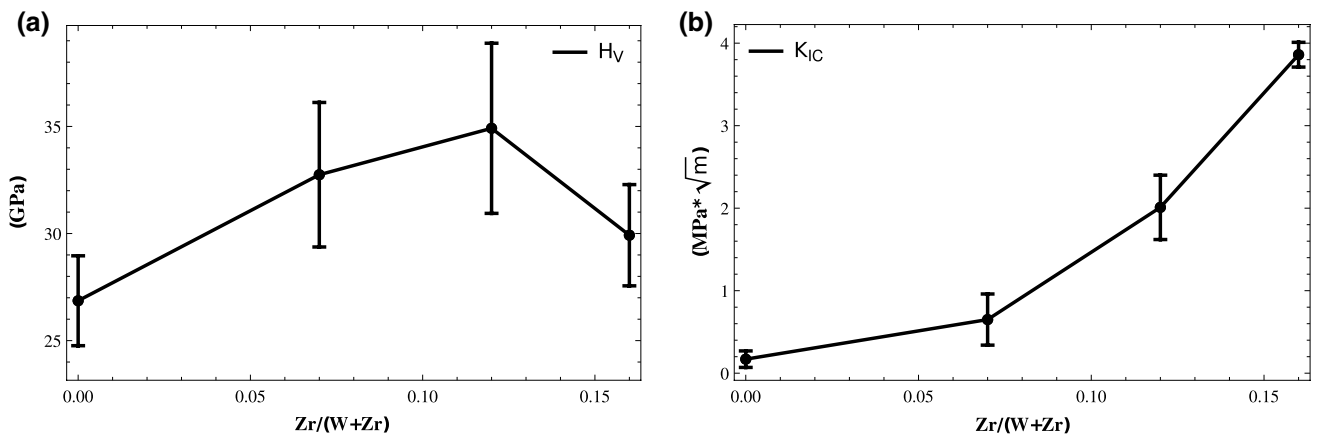

Fig. 7 Deposited $W - Zr - B_x$ films **a** Vickers hardness H_v (GPa), **b** fracture toughness K_{IC} (MPa$\sqrt{m}$)

simultaneous increase in hardness and fracture toughness [47]. In the presented case, $W-Zr-B_{2-x}$ films can possess such a structure. According to the ZrB_2-W_2B_5 phase diagram [48], the melting temperature for 16 mol% of ZrB_2 is 2200 °C. During the experiment, the substrate temperature was 500 °C and the pressure of *Ar* was 0.9 Pa during deposition. On the basis of Thornton's structural zone model (SZM) [49], deposited films are in the T-zone.

The differences in mechanical properties can be explained at both an atomic level and based on microstructure. The mechanical properties of the ternaries are highly sensitive to the vacancy concentration [12]. It can clearly be seen that, during deposition, a large amount of boron is lost, which causes the crystal lattice to be built with vacancies. Vacancies result in a reduction of Young's modulus, a decreased lattice parameter c and may even result in a strengthening of α-WB_{2-z} [50]. The dominant strengthening mechanism can be related to solid solution hardening effects. This mechanism consists of parelastic and dielastic contributions [5], resulting from the different lattice parameters and shear moduli of ZrB_2 and WB_2.

In Fig. 8, the characteristic part of the XRD diffractogram of the coatings deposited on Si (001) substrate revealed main diffraction peaks ranging from $2\Theta = 20°$ to 38°. Complete diffraction patterns and their detailed analysis were presented in [9]. In the case of WB_{2-z}, the coating at the peak positioned at 28.9° comes from the (0001) plane of the hexagonal AlB_2-type WB_2 (α-WB_2) and the peak positioned at 26° is derived from the (0004) plane of hexagonal MoB_2 -type WB_2 (ω-W_2B_5). Based on detailed deconvolution of the XRD diffractogram, the α-WB_2 to ω-W_2B_5 ratio is 4.8 and both phases have a similar crystal size of 37 ± 2 nm (calculated on the basis of the Scherrer formula). In the case of *Zr*-doped coatings, the ZrB_2 phase does not appear and the diffraction lines (related to α-WB_2 and ω-W_2B_5) are shifted towards a smaller 2Θ angle, due to the higher radius of zirconium than tungsten. The shift towards smaller angles increases with *Zr* content. Moreover, the α-WB_2 to ω-W_2B_5 ratio decrease with *Zr*. Similar behavior of an alloyed WB_{2-z} coating has been already observed by Moraes et al. [10]. Researchers indicate that the shift in diffraction lines is related to boron vacancies and the formation of a new phase, in our case the $W-Zr-B$ phase. The crystallite size of α -WB_2 and ω-W_2B_5 phases do not change significantly with *Zr* content and are 30 and 40 nm, respectively. In the XRD diffractogram, apart from narrow diffraction lines, a broad diffraction line at 2Θ between 22° and 46° was observed, indicating amorphous phase.

The presence of the amorphous phase is also confirmed by the STEM images that were taken in selective area electron diffraction (SAED) mode (Fig. 9). There are no visible diffraction spots and the amorphous halo is mainly observed. Similar results were obtained by Mościcki et al. [45] for WB_2 films alloyed with titanium. The presence of the amorphous structure in $W-Ti-B_{4-x}$ was confirmed by the additional fast Fourier transform (FTT), where blurred diffraction rings were recorded [45].

The higher H_v values of the deposited coatings are primarily attributed to solid-solution hardening and their narrow columns (the *Hall–Petch* effect) [46]. In Fig. 10, STEM images of the $WB_{1.59}$ and $W_{0.93}Zr_{0.07}B_{1.35}$ coating cross-sections are shown. The obtained structure confirmed the earlier calculations of crystallite size. The deposited coating is characterised by a columnar structure (Figs. 29, 12, 13, 14, 15, 16, 17, 18, 19, 20, 21, 22, 23, 24, 25, 26, 29, 28).

The XRD diffractogram (Fig. 8) shows that the films are mainly deposited with a 0001 crystallographic orientation. The columnar structure and the crystallographic orientation can strongly influence the mechanical properties of deposited films. Fuger et al. [14] showed that 0001 oriented WB_{2-x} films are superhard but hardness linearly

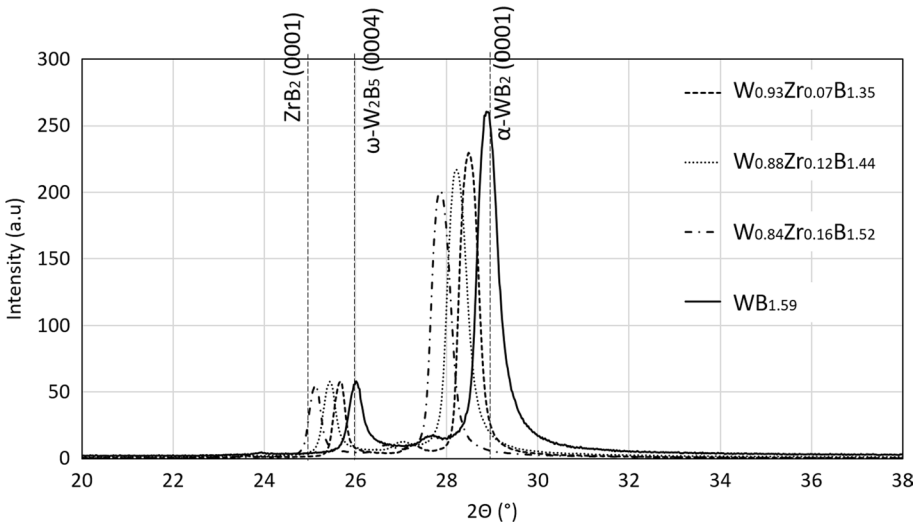

Fig. 8 Structural evolution of the $W_{1-x}Zr_xB_{2-z}$ coatings with increasing *Zr* content (x = 0.00, 0.07, 0.12, 0.16). The standardized 2Θ-peak positions of ω-W_2B_5 (a = 2.983Å, c = 13.879Å) [51], α-WB_2 (a = 3.020, c = 3.050) [52], α-ZrB_2 (a = 3.170Å, c = 3.548Å) [53] are indicated with a dashed lines

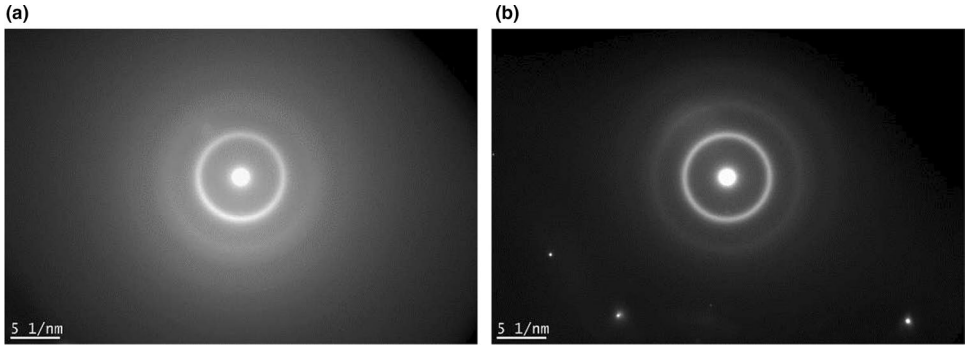

Fig. 9 STEM images in selective area electron diffraction (SAED) mode: **a** $WB_{1.59}$ and **b** $W_{0.93}Zr_{0.07}B_{1.35}$

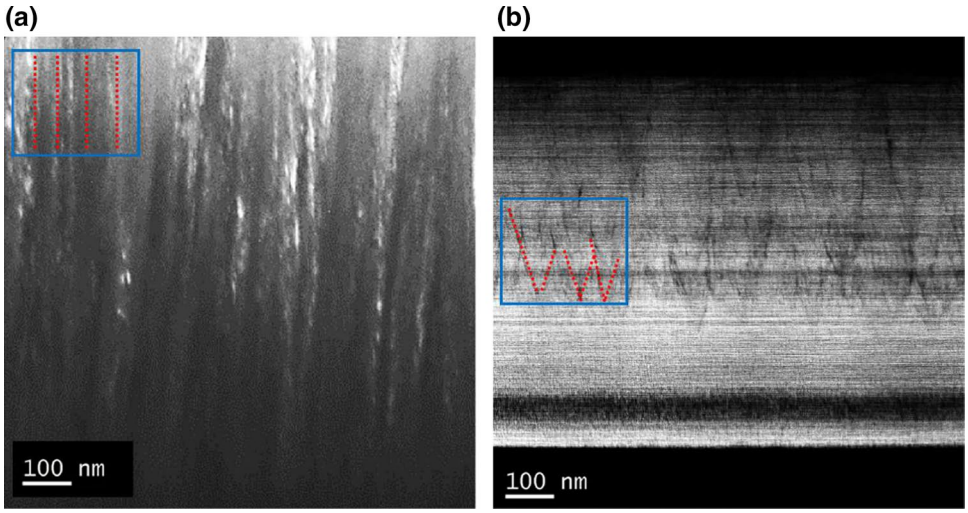

Fig. 10 BF STEM images of the cross-section of deposited layers: **a** $WB_{1.59}$ and **b** $W_{0.93}Zr_{0.07}B_{1.35}$. The blue insert shows the comparison with the structural zone models (SZM) of Barna and Adamik [54]

decreases by more than 15 GPa with an increasing $(10\bar{1}1)$ orientation. The STEM image of the $WB_{1.59}$ film's cross section, presented in Fig. 10a, shows a compact structure with elongated grains perpendicular to the substrate. A similar structure was presented in the case of magnetron sputtered hexagonal borides as TiB_2 [55] or $Zr_{1-x}Ta_xB_y$ [56]. Such films (where $0 \leq x \leq 0.1$) consist of columnar stoichiometric-diboride grains, encapsulated with a *B*-rich tissue phase, while alloy films (with $x \geq 0.2$) have a nanocolumnar structure with metal-rich boundaries. An increase in the tantalum content caused increased hardness due to solid-solution hardening, combined with a much smaller grain size (the *Hall–Petch* effect). Simultaneously, the increase of film fracture toughness was found, which can be explained because the metal-rich boundaries inhibit crack propagation, while allowing grain boundary sliding under heavy loads [56]. In the case of zirconium, the addition of a small amount of this element cased the change of columns direction and V-shaped grains were formed (Fig. 10b). Due to the structural zone models (SZM) of Barna and Adamik [54], such a shape is characteristic for 'Zone T', created when the impurity or additive content is growing. The grain boundary strengthening effect plays a greater role here. The reinforcing role of grain boundaries is that they act as barriers to dislocation movements, causing them to pile up. Plastic deformation cannot continue when the stresses reach the value necessary to initiate slip in the adjacent grain. The introducing of an irregular direction of columns increases strength in other directions, which can cause the increase in cracking resistance (K_{IC}).

4 Summary

Using quantum-mechanical calculations, the effect of *Zr* doping on the mechanical properties of $W_{1-x}Zr_xB_2$ was estimated. The results obtained by calculation were compared with experimental values measured on RF-magnetron sputtered coatings with similar compositions. Deposits of zirconium admixture films are characterized by a greater Vickers hardness H_v but lower fracture toughness K_{IC} than theoretical structures. Taking into account the fact that calculations were made for ideal cells and that there are several hardening mechanisms (not only solid solution hardening), the differences between the calculations and experimental test results can be significant. In addition, vacancies on boron position

and changes in microstructure (from columnar perpendicular to substrate to V-shaped grains) also influence the properties but are not included in the calculations. However, the results obtained predict new material that, due to its high hardness and improved brittle-ductile character, can be competitively utilized.

It can be concluded that

- DFT-calculated *Zr* doped tungsten diboride is mechanically and thermodynamically stable.
- DFT calculations show that zirconium doping reduces hardness and fracture toughness of hP6-P6$_3$/mmc-WB_2 but do not affect these properties in the case of hP3-P6/mmm.
- Introducing vacancies resulted in a significant decrease in hardness for hP6 and an increase for hP3.
- Magnetron sputtered tungsten–zirconium diboride $W_{1-x}Zr_xB_{2-y}$ ($x < 0.2$) belongs to superhard materials, in which an increase of fracture toughness is simultaneous with an increase in hardness.
- Obtained by DFT calculation, $W_{1-x}Zr_xB_{2-y}$ ($x < 0.2$) structures are not superhard. However, magnetron sputtering provides special conditions which cause films to be deposited with a (0001) orientation, which can possess Vickers hardness greater than 40 GPa due to solid solution hardening, the *Hall–Petch* effect and the growth of V-shaped grains.

Crystallographic information and stiffness tensors of $W_{1-x}Zr_xB_2$

WB_2

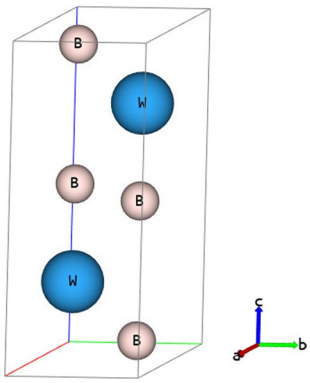

Fig. 11 WB_2: basic cell

WB2

_symmetry_space_group_name_H-M “P 63/m 2/m 2/c”
_symmetry_Int_Tables_number 194

_cell_length_a 2.89773
_cell_length_b 2.89773
_cell_length_c 7.67174
_cell_angle_alpha 90.00000
_cell_angle_beta 90.00000
_cell_angle_gamma 120.00000
_cell_volume 55.786499

loop_
_space_group_symop_id
_space_group_symop_operation_xyz
1 x,y,z
2 x-y,x,z+1/2
3 -y,x-y,z
4 -x,-y,z+1/2
5 -x+y,-x,z
6 y,-x+y,z+1/2
7 x-y,-y,-z
8 x,x-y,-z+1/2
9 y,x,-z
10 -x+y,y,-z+1/2
11 -x,-x+y,-z
12 -y,-x,-z+1/2
13 -x,-y,-z
14 -x+y,-x,-z+1/2
15 y,-x+y,-z
16 x,y,-z+1/2
17 x-y,x,-z
18 -y,x-y,-z+1/2
19 -x+y,y,z
20 -x,-x+y,z+1/2
21 -y,-x,z
22 x-y,-y,z+1/2
23 x,x-y,z
24 y,x,z+1/2

loop_
_atom_site_label
_atom_site_type_symbol
_atom_site_symmetry_multiplicity
_atom_site_Wyckoff_label
_atom_site_fract_x
_atom_site_fract_y
_atom_site_fract_z
_atom_site_occupancy
B1 B 4 f 0.33333 0.66667 0.04149 1.00000
W1 W 2 d 0.33333 0.66667 0.75000 1.00000

Stiffness tensor:

$$[C_{IJ}] \rightarrow \begin{vmatrix} 610.214 & 206.739 & 117.767 & 0.0 & 0.0 & 0.0 \\ 206.739 & 610.214 & 117.767 & 0.0 & 0.0 & 0.0 \\ 117.767 & 117.767 & 953.482 & 0.0 & 0.0 & 0.0 \\ 0.0 & 0.0 & 0.0 & 276.306 & 0.0 & 0.0 \\ 0.0 & 0.0 & 0.0 & 0.0 & 276.306 & 0.0 \\ 0.0 & 0.0 & 0.0 & 0.0 & 0.0 & 201.737 \end{vmatrix} \text{[GPa]}.$$

$W_{0.75}Zr_{0.25}B_2$

W3Zr1B8

_symmetry_space_group_name_H-M “P m m 2”
_symmetry_Int_Tables_number 25

_cell_length_a 2.92850
_cell_length_b 7.86539
_cell_length_c 5.09269
_cell_angle_alpha 90.00000
_cell_angle_beta 90.00000
_cell_angle_gamma 90.00000
_cell_volume 117.303970

loop_
_space_group_symop_id
_space_group_symop_operation_xyz
1 x,y,z
2 -x,-y,z
3 -x,y,z
4 x,-y,z

loop_
_atom_site_label
_atom_site_type_symbol
_atom_site_symmetry_multiplicity
_atom_site_Wyckoff_label
_atom_site_fract_x
_atom_site_fract_y
_atom_site_fract_z
_atom_site_occupancy
B1 B 2 h 0.50000 0.20119 0.16510 1.00000
B2 B 2 g 0.00000 0.72339 0.34035 1.00000
Zr1 Zr 1 d 0.50000 0.50000 0.16899 1.00000
W1 W 1 a 0.00000 0.00000 0.33328 1.00000
B3 B 2 g 0.00000 0.20557 0.66808 1.00000
B4 B 2 h 0.50000 0.71599 0.82637 1.00000
W2 W 1 b 0.00000 0.50000 0.66423 1.00000

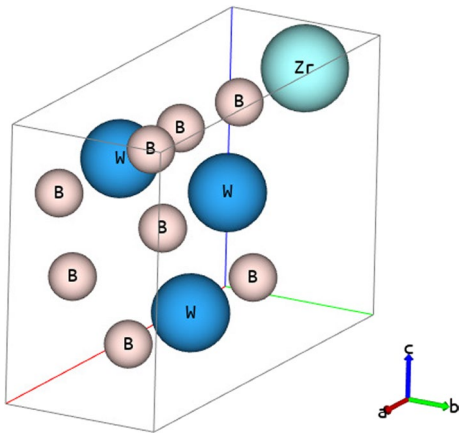

Fig. 12 $W_{0.75}Zr_{0.25}B_2$: basic cell

W3 W 1 c 0.50000 0.00000 0.83369 1.00000

Stiffness tensor:

$$[C_{IJ}] \rightarrow \begin{vmatrix} 478.007 & 182.029 & 104.013 & 0.0 & 0.0 & 0.0 \\ 182.029 & 460.394 & 100.821 & 0.0 & 0.0 & 0.0 \\ 104.013 & 100.821 & 778.679 & 0.0 & 0.0 & 0.0 \\ 0.0 & 0.0 & 0.0 & 199.078 & 0.0 & 0.0 \\ 0.0 & 0.0 & 0.0 & 0.0 & 200.996 & 0.0 \\ 0.0 & 0.0 & 0.0 & 0.0 & 0.0 & 143.843 \end{vmatrix} \text{[GPa]}.$$

$W_{0.835}Zr_{0.165}B_2$

W5Zr1B12

_symmetry_space_group_name_H-M “P 1 m 1”
_symmetry_Int_Tables_number 6

_cell_length_a 2.92020
_cell_length_b 7.79490
_cell_length_c 7.74161
_cell_angle_alpha 90.00000
_cell_angle_beta 100.86151
_cell_angle_gamma 90.00000
_cell_volume 173.062812

loop_
_space_group_symop_id
_space_group_symop_operation_xyz
1 x,y,z
2 x,-y,z

loop_
_atom_site_label
_atom_site_type_symbol
_atom_site_symmetry_multiplicity
_atom_site_Wyckoff_label
_atom_site_fract_x
_atom_site_fract_y
_atom_site_fract_z
_atom_site_occupancy
B1 B 2 c 0.55506 0.70158 0.11007 1.00000
B2 B 2 c 0.11408 0.22189 0.22820 1.00000
Zr1 Zr 1 a 0.55643 0.00000 0.11321 1.00000
W1 W 1 b 0.11201 0.50000 0.22382 1.00000
B3 B 2 c 0.22357 0.70665 0.44711 1.00000
B4 B 2 c 0.77735 0.21081 0.55471 1.00000
W2 W 1 a 0.22479 0.00000 0.44974 1.00000
W3 W 1 b 0.77804 0.50000 0.55587 1.00000
B5 B 2 c 0.88801 0.70716 0.77598 1.00000
B6 B 2 c 0.44182 0.21480 0.88365 1.00000
W4 W 1 a 0.88523 0.00000 0.77078 1.00000
W5 W 1 b 0.44373 0.50000 0.88715 1.00000

_space_group_symop_operation_xyz
1 x,y,z
2 -x,-y,z
3 x,-y,z
4 -x,y,z
5 x,y+1/2,z+1/2
6 -x,-y+1/2,z+1/2
7 x,-y+1/2,z+1/2
8 -x,y+1/2,z+1/2

loop_
_atom_site_label
_atom_site_type_symbol
_atom_site_symmetry_multiplicity
_atom_site_Wyckoff_label
_atom_site_fract_x
_atom_site_fract_y
_atom_site_fract_z
_atom_site_occupancy
B1 B 8 f 0.29282 0.25106 0.41635 1.00000

Stiffness tensor:

$$[\mathbf{C_{IJ}}] \rightarrow \begin{bmatrix} 492.413 & 193.593 & 107.138 & 0.0 & 0.0 & 9.467 \\ 193.593 & 523.859 & 113.458 & 0.0 & 0.0 & 0.231 \\ 107.138 & 113.458 & 846.563 & 0.0 & 0.0 & -0.362 \\ 0.0 & 0.0 & 0.0 & 224.912 & -0.623 & 0.0 \\ 0.0 & 0.0 & 0.0 & -0.623 & 217.7 & 0.0 \\ 9.467 & 0.231 & -0.362 & 0.0 & 0.0 & 157.822 \end{bmatrix} \text{[GPa].}$$

$W_{0.875}Zr_{0.125}B_2$

W7Zr1B16

_symmetry_space_group_name_H-M “A m m 2”
_symmetry_Int_Tables_number 38

_cell_length_a 7.76000
_cell_length_b 5.83172
_cell_length_c 10.11121
_cell_angle_alpha 90.00000
_cell_angle_beta 90.00000
_cell_angle_gamma 90.00000
_cell_volume 457.574184

loop_
_space_group_symop_id

B2 B 8 f 0.78400 0.74474 0.08156 1.00000
W1 W 4 d 0.00000 0.74875 -0.08290 1.00000
W2 W 4 e 0.50000 0.25016 0.58337 1.00000
B3 B 4 c 0.29283 0.00000 0.66740 1.00000
B4 B 4 c 0.79218 0.00000 0.83330 1.00000
W3 W 2 a 0.00000 0.00000 0.66585 1.00000
W4 W 2 b 0.50000 0.00000 0.83332 1.00000
B5 B 4 c 0.29747 0.00000 0.16668 1.00000
B6 B 4 c 0.78398 0.00000 0.33681 1.00000
Zr1 Zr 2 a 0.00000 0.00000 0.16669 1.00000
W5 W 2 b 0.50000 0.00000 0.33320 1.00000

Stiffness tensor:

$$[\mathbf{C_{IJ}}] \rightarrow \begin{vmatrix} 541.56 & 200.813 & 111.13 & 0.0 & 0.0 & 0.0 \\ 200.813 & 532.753 & 112.813 & 0.0 & 0.0 & 0.0 \\ 111.13 & 112.813 & 852.923 & 0.0 & 0.0 & 0.0 \\ 0.0 & 0.0 & 0.0 & 231.813 & 0.0 & 0.0 \\ 0.0 & 0.0 & 0.0 & 0.0 & 229.596 & 0.0 \\ 0.0 & 0.0 & 0.0 & 0.0 & 0.0 & 166.8 \end{vmatrix} \text{[GPa].}$$

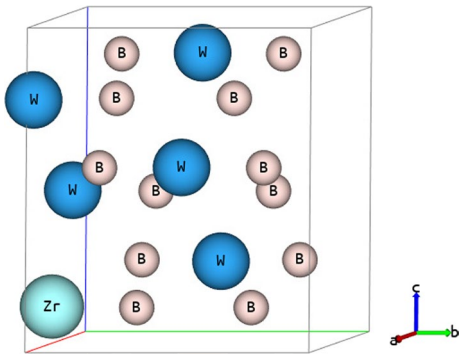

Fig. 13 $W_{0.835}Zr_{0.165}B_2$: basic cell

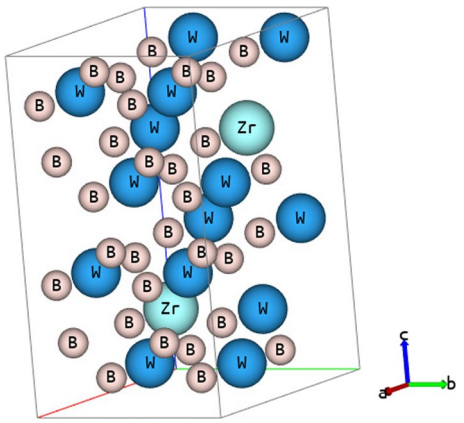

Fig. 14 $W_{0.875}Zr_{0.125}B_2$: basic cell

$W_{0.915}Zr_{0.085}B_2$

W11Zr1B24

_symmetry_space_group_name_H-M “P 1 m 1”
_symmetry_Int_Tables_number 6

_cell_length_a 5.81990
_cell_length_b 7.72960
_cell_length_c 7.70561
_cell_angle_alpha 90.00000
_cell_angle_beta 100.89389
_cell_angle_gamma 90.00000
_cell_volume 340.393845

loop_
_space_group_symop_id

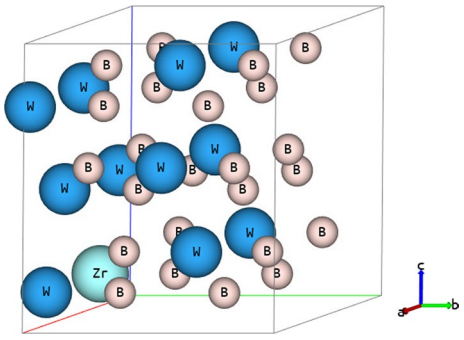

Fig. 15 $W_{0.915}Zr_{0.085}B_2$: basic cell

_space_group_symop_operation_xyz
1 x,y,z
2 x,-y,z

loop_
_atom_site_label
_atom_site_type_symbol
_atom_site_symmetry_multiplicity
_atom_site_Wyckoff_label
_atom_site_fract_x
_atom_site_fract_y
_atom_site_fract_z
_atom_site_occupancy
B1 B 2 c 0.77759 0.70726 0.11041 1.00000
B2 B 2 c 0.05107 0.21540 0.22524 1.00000
W1 W 1 a 0.77811 0.00000 0.11275 1.00000
W2 W 1 b 0.05560 0.50000 0.22304 1.00000
B3 B 2 c 0.11111 0.70770 0.44580 1.00000
B4 B 2 c 0.38864 0.20899 0.55470 1.00000
W3 W 1 a 0.10949 0.00000 0.44668 1.00000
W4 W 1 b 0.38932 0.50000 0.55473 1.00000
B5 B 2 c 0.44551 0.70785 0.77656 1.00000
B6 B 2 c 0.72216 0.20781 0.88918 1.00000
W5 W 1 a 0.44474 0.00000 0.77456 1.00000
W6 W 1 b 0.72200 0.50000 0.88888 1.00000
B7 B 2 c 0.27774 0.70280 0.11087 1.00000
B8 B 2 c 0.56161 0.21528 0.22527 1.00000
Zr1 Zr 1 a 0.27777 0.00000 0.11090 1.00000
W7 W 1 b 0.55593 0.50000 0.22290 1.00000
B9 B 2 c 0.61172 0.70767 0.44566 1.00000
B10 B 2 c 0.88896 0.21029 0.55570 1.00000
W8 W 1 a 0.61409 0.00000 0.44783 1.00000
W9 W 1 b 0.88852 0.50000 0.55665 1.00000
B11 B 2 c -0.05709 0.70776 0.77719 1.00000
B12 B 2 c 0.22101 0.21505 0.88330 1.00000
W10 W 1 a -0.05771 0.00000 0.77397 1.00000

W11 W 1 b 0.22210 0.50000 0.88735 1.00000

Stiffness tensor:

$$[C_{IJ}] \rightarrow \begin{bmatrix} 530.328 & 186.025 & 114.522 & 0.0 & 0.0 & -9.041 \\ 186.025 & 480.47 & 113.165 & 0.0 & 0.0 & -4.657 \\ 114.522 & 113.165 & 879.372 & 0.0 & 0.0 & -11.539 \\ 0.0 & 0.0 & 0.0 & 240.626 & -11.962 & 0.0 \\ 0.0 & 0.0 & 0.0 & -11.962 & 239.934 & 0.0 \\ -9.041 & -4.657 & -11.539 & 0.0 & 0.0 & 156.3 \end{bmatrix} \text{[GPa]}.$$

$W_{0.937}Zr_{0.063}B_2$

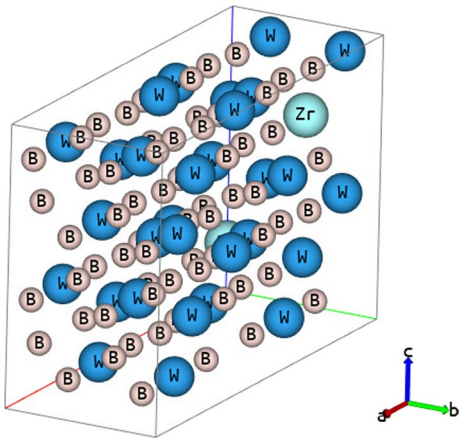

Fig. 16 $W_{0.937}Zr_{0.063}B_2$: basic cell

W15Zr1B32

_symmetry_space_group_name_H-M “A m m 2”
_symmetry_Int_Tables_number 38

_cell_length_a 15.43145
_cell_length_b 5.81311
_cell_length_c 10.07829
_cell_angle_alpha 90.00000
_cell_angle_beta 90.00000
_cell_angle_gamma 90.00000
_cell_volume 904.0701

loop_
_space_group_symop_id
_space_group_symop_operation_xyz
1 x,y,z
2 -x,-y,z
3 x,-y,z
4 -x,y,z
5 x,y+1/2,z+1/2
6 -x,-y+1/2,z+1/2
7 x,-y+1/2,z+1/2
8 -x,y+1/2,z+1/2

loop_
_atom_site_label
_atom_site_type_symbol
_atom_site_symmetry_multiplicity
_atom_site_Wyckoff_label
_atom_site_fract_x
_atom_site_fract_y
_atom_site_fract_z
_atom_site_occupancy
B1 B 8 f 0.14734 0.25081 0.41643 1.00000
B2 B 8 f 0.89112 0.74498 0.08163 1.00000
B3 B 8 f 0.35518 0.25026 0.41660 1.00000
W1 W 4 d 0.00000 0.74863 -0.08287 1.00000
W2 W 8 f 0.25182 0.75006 0.08334 1.00000
B4 B 4 c 0.14734 0.00000 0.66722 1.00000
B5 B 4 c 0.89566 0.00000 0.83330 1.00000
B6 B 4 c 0.35518 0.00000 0.66687 1.00000
W3 W 2 a 0.00000 0.00000 0.66576 1.00000
W4 W 4 c 0.25085 0.00000 0.83332 1.00000
B7 B 4 c 0.15001 0.00000 0.16668 1.00000
B8 B 4 c 0.89112 0.00000 0.33665 1.00000
B9 B 4 c 0.35554 0.00000 0.16669 1.00000
Zr1 Zr 2 a 0.00000 0.00000 0.16669 1.00000
W5 W 4 c 0.25181 0.00000 0.33327 1.00000
B10 B 8 f 0.39658 0.74992 0.08329 1.00000
W6 W 4 e 0.50000 0.75010 -0.08334 1.00000
B11 B 4 c 0.39620 0.00000 0.83331 1.00000
W7 W 2 b 0.50000 0.00000 0.66675 1.00000
B12 B 4 c 0.39658 0.00000 0.33336 1.00000
W8 W 2 b 0.50000 0.00000 0.16669 1.00000

Stiffness tensor:

$$[C_{IJ}] \rightarrow \begin{bmatrix} 550.316 & 201.993 & 112.048 & 0.0 & 0.0 & 0.0 \\ 201.993 & 557.618 & 112.261 & 0.0 & 0.0 & 0.0 \\ 112.048 & 112.261 & 891.579 & 0.0 & 0.0 & 0.0 \\ 0.0 & 0.0 & 0.0 & 243.58 & 0.0 & 0.0 \\ 0.0 & 0.0 & 0.0 & 0.0 & 242.94 & 0.0 \\ 0.0 & 0.0 & 0.0 & 0.0 & 0.0 & 175.921 \end{bmatrix} \text{[GPa]}.$$

$W_{0.944}Zr_{0.056}B_2$

W17Zr1B36

_symmetry_space_group_name_H-M “A m m 2”
_symmetry_Int_Tables_number 38

_cell_length_a 7.71029
_cell_length_b 8.71823
_cell_length_c 15.10683
_cell_angle_alpha 90.00000
_cell_angle_beta 90.00000
_cell_angle_gamma 90.00000
_cell_volume 1015.4823

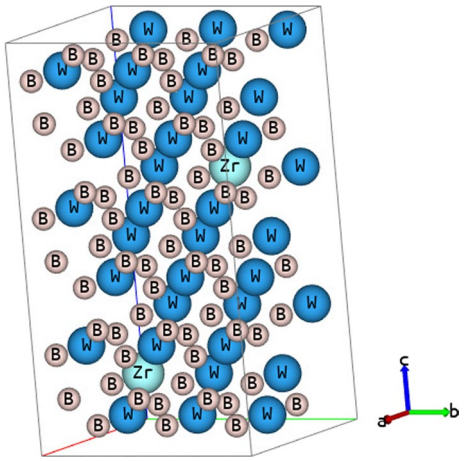

Fig. 17 $W_{0.944}Zr_{0.056}B_2$: basic cell

loop_
_space_group_symop_id
_space_group_symop_operation_xyz
1 x,y,z
2 -x,-y,z
3 x,-y,z
4 -x,y,z
5 x,y+1/2,z+1/2
6 -x,-y+1/2,z+1/2
7 x,-y+1/2,z+1/2
8 -x,y+1/2,z+1/2

loop_
_atom_site_label
_atom_site_type_symbol
_atom_site_symmetry_multiplicity
_atom_site_Wyckoff_label
_atom_site_fract_x
_atom_site_fract_y
_atom_site_fract_z
_atom_site_occupancy
B1 B 8 f 0.29218 0.33311 0.44380 1.00000
B2 B 8 f 0.78523 0.82923 0.05418 1.00000
W1 W 4 d 0.00000 0.83127 -0.05695 1.00000
W2 W 4 e 0.50000 0.33237 0.55523 1.00000
B3 B 8 f 0.29220 0.66557 0.11133 1.00000
B4 B 8 f 0.79170 0.66674 0.22219 1.00000
W3 W 4 d 0.00000 0.16352 0.61079 1.00000
W4 W 4 e 0.50000 0.16644 0.72228 1.00000
B5 B 4 c 0.29151 0.00000 0.77778 1.00000
B6 B 4 c 0.79170 0.00000 0.88893 1.00000
W5 W 2 a 0.00000 0.00000 0.77780 1.00000
W6 W 2 b 0.50000 0.00000 0.88874 1.00000
B7 B 8 f 0.29219 0.16754 0.27822 1.00000
B8 B 8 f 0.79023 0.16613 0.38906 1.00000
W7 W 4 d 0.00000 0.66775 0.77953 1.00000
W8 W 4 e 0.50000 0.66662 0.88890 1.00000
B9 B 4 c 0.29180 0.00000 0.44445 1.00000
B10 B 4 c 0.79024 0.00000 0.55519 1.00000
W9 W 2 a 0.00000 0.00000 0.44445 1.00000
W10 W 2 b 0.50000 0.00000 0.55550 1.00000
B11 B 4 c 0.29703 0.00000 0.11111 1.00000
B12 B 4 c 0.78522 0.00000 0.22495 1.00000
Zr1 Zr 2 a 0.00000 0.00000 0.11113 1.00000
W11 W 2 b 0.50000 0.00000 0.22285 1.00000

Stiffness tensor:

$$[\mathbf{C_{IJ}}] \rightarrow \begin{bmatrix} 556.402 & 204.376 & 119.244 & 0.0 & 0.0 & 0.0 \\ 204.376 & 552.65 & 119.067 & 0.0 & 0.0 & 0.0 \\ 119.244 & 119.067 & 919.327 & 0.0 & 0.0 & 0.0 \\ 0.0 & 0.0 & 0.0 & 252.179 & 0.0 & 0.0 \\ 0.0 & 0.0 & 0.0 & 0.0 & 251.884 & 0.0 \\ 0.0 & 0.0 & 0.0 & 0.0 & 0.0 & 179.463 \end{bmatrix} \text{[GPa]}.$$

$W_{0.958}Zr_{0.042}B_2$

W23Zr1B48

_symmetry_space_group_name_H-M “P 1 m 1”
_symmetry_Int_Tables_number 6

_cell_length_a 5.85400
_cell_length_b 15.49600
_cell_length_c 7.74411
_cell_angle_alpha 90.00000
_cell_angle_beta 100.89339
_cell_angle_gamma 90.00000
_cell_volume 689.837402

loop_
_space_group_symop_id
_space_group_symop_operation_xyz
1 x,y,z
2 x,-y,z

loop_
_atom_site_label
_atom_site_type_symbol
_atom_site_symmetry_multiplicity
_atom_site_Wyckoff_label
_atom_site_fract_x
_atom_site_fract_y
_atom_site_fract_z
_atom_site_occupancy
B1 B 2 c 0.77778 0.35450 0.11111 1.00000
B2 B 2 c 0.05555 0.60450 0.22222 1.00000
B3 B 2 c 0.77778 0.14550 0.11111 1.00000
W1 W 1 b 0.77778 0.50000 0.11111 1.00000
W2 W 2 c 0.05555 0.25000 0.22222 1.00000
B4 B 2 c 0.11111 0.35450 0.44444 1.00000
B5 B 2 c 0.38889 0.60450 0.55556 1.00000
B6 B 2 c 0.11111 0.14550 0.44444 1.00000
W3 W 1 b 0.11111 0.50000 0.44444 1.00000
W4 W 2 c 0.38889 0.25000 0.55556 1.00000
B7 B 2 c 0.44445 0.35450 0.77778 1.00000
B8 B 2 c 0.72222 0.60450 0.88889 1.00000
B9 B 2 c 0.44445 0.14550 0.77778 1.00000
W5 W 1 b 0.44445 0.50000 0.77778 1.00000
W6 W 2 c 0.72222 0.25000 0.88889 1.00000
B10 B 2 c 0.27778 0.35450 0.11111 1.00000
B11 B 2 c 0.55555 0.60450 0.22222 1.00000
B12 B 2 c 0.27778 0.14550 0.11111 1.00000
Zr1 Zr 1 b 0.27778 0.50000 0.11111 1.00000
W7 W 2 c 0.55555 0.25000 0.22222 1.00000
B13 B 2 c 0.61111 0.35450 0.44444 1.00000
B14 B 2 c 0.88889 0.60450 0.55556 1.00000
B15 B 2 c 0.61111 0.14550 0.44444 1.00000
W8 W 1 b 0.61111 0.50000 0.44444 1.00000
W9 W 2 c 0.88889 0.25000 0.55556 1.00000
B16 B 2 c -0.05555 0.35450 0.77778 1.00000
B17 B 2 c 0.22222 0.60450 0.88889 1.00000
B18 B 2 c -0.05555 0.14550 0.77778 1.00000
W10 W 1 b -0.05555 0.50000 0.77778 1.00000
W11 W 2 c 0.22222 0.25000 0.88889 1.00000
B19 B 2 c 0.05555 0.10450 0.22222 1.00000
W12 W 1 a 0.77778 0.00000 0.11111 1.00000
B20 B 2 c 0.38889 0.10450 0.55556 1.00000
W13 W 1 a 0.11111 0.00000 0.44444 1.00000
B21 B 2 c 0.72222 0.10450 0.88889 1.00000
W14 W 1 a 0.44445 0.00000 0.77778 1.00000
B22 B 2 c 0.55555 0.10450 0.22222 1.00000
W15 W 1 a 0.27778 0.00000 0.11111 1.00000
B23 B 2 c 0.88889 0.10450 0.55556 1.00000
W16 W 1 a 0.61111 0.00000 0.44444 1.00000
B24 B 2 c 0.22222 0.10450 0.88889 1.00000
W17 W 1 a -0.05555 0.00000 0.77778 1.00000

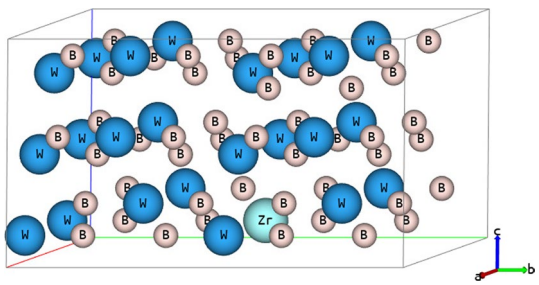

Fig. 18 $W_{0.958}Zr_{0.042}B_2$: basic cell

Stiffness tensor:

$$[C_{IJ}] \rightarrow \begin{bmatrix} 537.192 & 197.719 & 117.261 & 0.0 & 0.0 & -6.457 \\ 197.719 & 545.365 & 112.046 & 0.0 & 0.0 & -12.885 \\ 117.261 & 112.046 & 910.756 & 0. & 0. & -0.329 \\ 0.0 & 0.0 & 0.0 & 248.433 & -0.956 & 0.0 \\ 0.0 & 0.0 & 0.0 & -0.956 & 252.497 & 0.0 \\ -6.457 & -12.885 & -0.329 & 0.0 & 0.0 & 174.342 \end{bmatrix} \text{[GPa]}.$$

$W_{0.969}Zr_{0.031}B_2$

W31Zr1B64

_symmetry_space_group_name_H-M “A m m 2”
_symmetry_Int_Tables_number 38

_cell_length_a 7.69207
_cell_length_b 11.61541
_cell_length_c 20.11349
_cell_angle_alpha 90.00000
_cell_angle_beta 90.00000
_cell_angle_gamma 90.00000
_cell_volume 1797.077344

loop_
_space_group_symop_id
_space_group_symop_operation_xyz
1 x,y,z
2 -x,-y,z
3 x,-y,z
4 -x,y,z
5 x,y+1/2,z+1/2
6 -x,-y+1/2,z+1/2
7 x,-y+1/2,z+1/2
8 -x,y+1/2,z+1/2

loop_
_atom_site_label
_atom_site_type_symbol
_atom_site_symmetry_multiplicity
_atom_site_Wyckoff_label
_atom_site_fract_x
_atom_site_fract_y
_atom_site_fract_z
_atom_site_occupancy
B1 B 8 f 0.29214 0.37456 0.45764 1.00000
B2 B 8 f 0.78531 0.87170 0.04057 1.00000
W1 W 4 d 0.00000 0.87339 -0.04271 1.00000
W2 W 4 e 0.50000 0.37399 0.54134 1.00000
B3 B 8 f 0.29214 0.74874 0.08346 1.00000
B4 B 8 f 0.79190 0.75000 0.16667 1.00000
W3 W 4 d 0.00000 0.24762 0.58305 1.00000
W4 W 4 e 0.50000 0.24975 0.66675 1.00000
B5 B 8 f 0.29145 0.62487 0.20837 1.00000
B6 B 8 f 0.79132 0.62495 0.29165 1.00000
W5 W 4 d 0.00000 0.12476 0.70841 1.00000
W6 W 4 e 0.50000 0.12487 0.79163 1.00000
B7 B 4 c 0.29145 0.00000 0.83325 1.00000
B8 B 4 c 0.79190 0.00000 -0.08333 1.00000
W7 W 2 a 0.00000 0.00000 0.83317 1.00000
W8 W 2 b 0.50000 0.00000 -0.08349 1.00000
B9 B 8 f 0.29157 0.25012 0.33329 1.00000
B10 B 8 f 0.79094 0.24937 0.41648 1.00000
W9 W 4 d 0.00000 0.75000 0.83333 1.00000
W10 W 4 e 0.50000 0.74939 -0.08374 1.00000
B11 B 8 f 0.29157 0.12473 0.45824 1.00000
B12 B 8 f 0.79094 0.62439 0.04145 1.00000
W11 W 4 d 0.00000 0.62450 -0.04183 1.00000
W12 W 4 e 0.50000 0.12408 0.54157 1.00000
B13 B 4 c 0.29157 0.00000 0.58341 1.00000
B14 B 4 c 0.79132 0.00000 0.66671 1.00000
W13 W 2 a 0.00000 0.00000 0.58333 1.00000

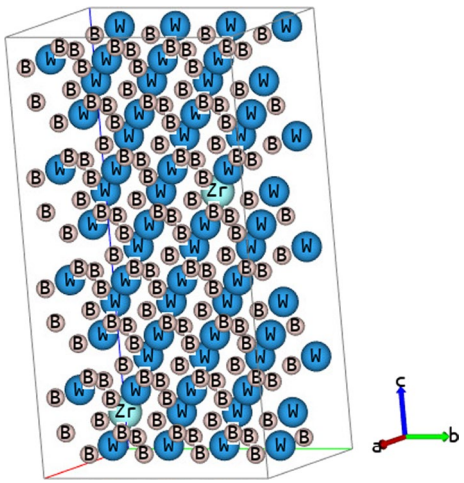

Fig. 19 $W_{0.969}Zr_{0.031}B_2$: basic cell

W14 W 2 b 0.50000 0.00000 0.66676 1.00000
B15 B 8 f 0.29214 0.12582 0.20890 1.00000
B16 B 8 f 0.79094 0.12498 0.29208 1.00000
W15 W 4 d 0.00000 0.62577 0.70965 1.00000
W16 W 4 e 0.50000 0.62532 0.79218 1.00000
B17 B 4 c 0.29157 0.00000 0.33351 1.00000
B18 B 4 c 0.79114 0.00000 0.41667 1.00000
W17 W 2 a 0.00000 0.00000 0.33366 1.00000
W18 W 2 b 0.50000 0.00000 0.41667 1.00000
B19 B 4 c 0.29718 0.00000 0.08333 1.00000
B20 B 4 c 0.78532 0.00000 0.16887 1.00000
Zr1 Zr 2 a 0.00000 0.00000 0.08333 1.00000
W19 W 2 b 0.50000 0.00000 0.16735 1.00000

Stiffness tensor:

$$[\mathbf{C_{IJ}}] \rightarrow \begin{bmatrix} 538.607 & 197.882 & 116.845 & 0.0 & 0.0 & 0.0 \\ 197.882 & 551.257 & 117.099 & 0.0 & 0.0 & 0.0 \\ 116.845 & 117.099 & 926.041 & 0.0 & 0.0 & 0.0 \\ 0.0 & 0.0 & 0.0 & 254.858 & 0.0 & 0.0 \\ 0.0 & 0.0 & 0.0 & 0.0 & 254.479 & 0.0 \\ 0.0 & 0.0 & 0.0 & 0.0 & 0.0 & 175.458 \end{bmatrix} \text{[GPa].}$$

$W_{0.857}Zr_{0.143}B_2$

W6Zr1B14

_symmetry_space_group_name_H-M “P 1”
_symmetry_Int_Tables_number 1

_cell_length_a 5.80809
_cell_length_b 5.86130
_cell_length_c 7.61578
_cell_angle_alpha 90.07497
_cell_angle_beta 90.00338
_cell_angle_gamma 119.65691
_cell_volume 225.300872

loop_
_space_group_symop_id
_space_group_symop_operation_xyz
1 x,y,z

loop_
_atom_site_label
_atom_site_type_symbol
_atom_site_symmetry_multiplicity
_atom_site_Wyckoff_label
_atom_site_fract_x
_atom_site_fract_y
_atom_site_fract_z
_atom_site_occupancy
B1 B 1 a 0.83141 0.63953 0.45406 1.00000
B2 B 1 a 0.16812 0.81265 0.53352 1.00000
B3 B 1 a 0.74214 0.59922 0.03493 1.00000
W1 W 1 a 0.84044 0.64561 0.74087 1.00000
B4 B 1 a 0.33173 0.63944 0.45404 1.00000
B5 B 1 a 0.67330 0.82327 -0.05342 1.00000
B6 B 1 a 0.66605 0.80870 0.53891 1.00000
W2 W 1 a 0.32892 0.64549 0.74081 1.00000
W3 W 1 a 0.66199 0.80066 0.25034 1.00000
B7 B 1 a 0.33480 0.14590 0.46734 1.00000
B8 B 1 a 0.77796 0.36104 -0.03921 1.00000
B9 B 1 a 0.66897 0.31075 0.53952 1.00000
B10 B 1 a 0.38100 0.59853 0.03487 1.00000
Zr1 Zr 1 a 0.33302 0.14213 0.79112 1.00000
W4 W 1 a 0.65331 0.31090 0.25192 1.00000
B11 B 1 a 0.83250 0.14127 0.45271 1.00000
B12 B 1 a 0.10674 0.36105 -0.03924 1.00000
B13 B 1 a 0.16538 0.31079 0.53959 1.00000
B14 B 1 a 0.82474 0.12549 0.05373 1.00000
W5 W 1 a 0.83173 0.13962 0.74275 1.00000
W6 W 1 a 0.18110 0.31075 0.25200 1.00000

Stiffness tensor:

$$[\mathbf{C_{IJ}}] \rightarrow \begin{bmatrix} 337.2 & 165.0 & 114.1 & 0. & 0.0 & -8.8 \\ 165.0 & 390.3 & 126.5 & -0.03 & 0.0 & -15.8 \\ 114.1 & 126.5 & 549.5 & -0.238 & -0.01 & 0.0 \\ 0.0 & -0.03 & -0.238 & 167.6 & 0.0 & 0.0 \\ 0.0 & 0.0 & -0.01 & 0.0 & 90.9 & 0.036 \\ -8.8 & -15.8 & 0.0 & 0.0 & 0.036 & 101.2 \end{bmatrix} \text{[GPa].}$$

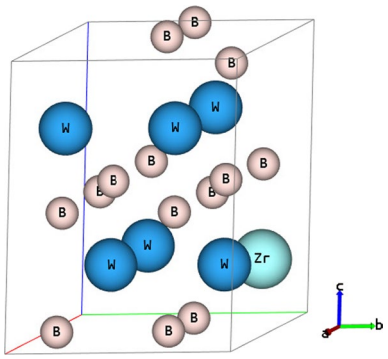

Fig. 20 $W_{0.857}Zr_{0.143}B_2$: basic cell

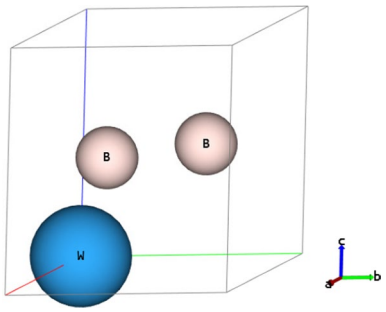

Fig. 21 WB_2: basic cell

WB_2

W1B2

_symmetry_space_group_name_H-M 'P 6/m m m'
_symmetry_Int_Tables_number 191
_cell_length_a 3.02238641
_cell_length_b 3.02238641
_cell_length_c 3.38202900
_cell_angle_alpha 90.00000000
_cell_angle_beta 90.00000000
_cell_angle_gamma 120.00000000
_cell_volume 26.75518352

loop_
_atom_site_label
_atom_site_fract_x
_atom_site_fract_y
_atom_site_fract_z
W 0.0000 0.0000 0.0000
B 0.3333 0.6667 0.5000

Stiffness tensor:

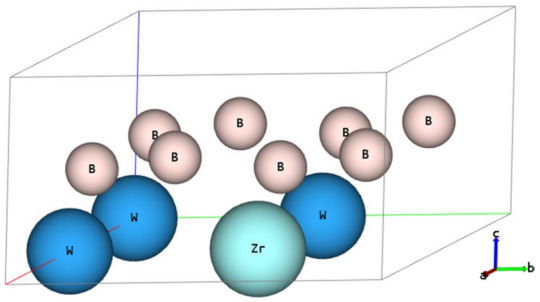

Fig. 22 $W_{0.75}Zr_{0.25}B_2$: basic cell

$$[C_{IJ}] \rightarrow \begin{bmatrix} 593.75 & 163.0 & 271.8 & 0.0 & 0.0 & 0.0 \\ 163.0 & 593.75 & 271.8 & 0.0 & 0.0 & 0.0 \\ 271.8 & 271.8 & 449.0 & 0.0 & 0.0 & 0.0 \\ 0.0 & 0.0 & 0.0 & 145.65 & 0.0 & 0.0 \\ 0.0 & 0.0 & 0.0 & 0.0 & 145.65 & 0.0 \\ 0.0 & 0.0 & 0.0 & 0.0 & 0.0 & 215.375 \end{bmatrix} \text{[GPa]}.$$

$W_{0.75}Zr_{0.25}B_2$

W3Zr1B8

_symmetry_space_group_name_H-M "P 6/m 2/m 2/m"
_symmetry_Int_Tables_number 191

_cell_length_a 6.06308
_cell_length_b 6.06308
_cell_length_c 3.34906
_cell_angle_alpha 90.00000
_cell_angle_beta 90.00000
_cell_angle_gamma 120.00000
_cell_volume 106.620359

loop_
_space_group_symop_id
_space_group_symop_operation_xyz
1 x,y,z
2 x-y,x,z
3 -y,x-y,z
4 -x,-y,z
5 -x+y,-x,z
6 y,-x+y,z
7 x-y,-y,-z
8 x,x-y,-z
9 y,x,-z
10 -x+y,y,-z
11 -x,-x+y,-z

12 -y,-x,-z
13 -x,-y,-z
14 -x+y,-x,-z
15 y,-x+y,-z
16 x,y,-z
17 x-y,x,-z
18 -y,x-y,-z
19 -x+y,y,z
20 -x,-x+y,z
21 -y,-x,z
22 x-y,-y,z
23 x,x-y,z
24 y,x,z

loop_
_atom_site_label
_atom_site_type_symbol
_atom_site_symmetry_multiplicity
_atom_site_Wyckoff_label
_atom_site_fract_x
_atom_site_fract_y
_atom_site_fract_z
_atom_site_occupancy
B1 B 6 m 0.16907 0.33815 0.50000 1.00000
W1 W 3 f 0.50000 0.00000 0.00000 1.00000
B2 B 2 d 0.33333 0.66667 0.50000 1.00000
Zr1 Zr 1 a 0.00000 0.00000 0.00000 1.00000

Stiffness tensor:

$$[\mathbf{C_{IJ}}] \rightarrow \begin{bmatrix} 625.232 & 125.859 & 225.863 & 0.0 & 0.0 & 0.0 \\ 125.859 & 625.232 & 225.863 & 0.0 & 0.0 & 0.0 \\ 225.863 & 225.863 & 431.445 & 0.0 & 0.0 & 0.0 \\ 0.0 & 0.0 & 0.0 & 194.511 & 0.0 & 0.0 \\ 0.0 & 0.0 & 0.0 & 0.0 & 194.511 & 0.0 \\ 0.0 & 0.0 & 0.0 & 0.0 & 0.0 & 249.686 \end{bmatrix} \text{[GPa].}$$

$W_{0.875}Zr_{0.125}B_2$

W7Zr1B16

_symmetry_space_group_name_H-M “P 6/m 2/m 2/m”
_symmetry_Int_Tables_number 191

_cell_length_a 6.04211
_cell_length_b 6.04211
_cell_length_c 6.65162
_cell_angle_alpha 90.00000
_cell_angle_beta 90.00000
_cell_angle_gamma 120.00000
_cell_volume 210.298080

loop_
_space_group_symop_id
_space_group_symop_operation_xyz
1 x,y,z
2 x-y,x,z
3 -y,x-y,z
4 -x,-y,z
5 -x+y,-x,z
6 y,-x+y,z
7 x-y,-y,-z
8 x,x-y,-z
9 y,x,-z
10 -x+y,y,-z
11 -x,-x+y,-z
12 -y,-x,-z
13 -x,-y,-z
14 -x+y,-x,-z
15 y,-x+y,-z
16 x,y,-z
17 x-y,x,-z
18 -y,x-y,-z
19 -x+y,y,z
20 -x,-x+y,z
21 -y,-x,z
22 x-y,-y,z
23 x,x-y,z
24 y,x,z

loop_
_atom_site_label
_atom_site_type_symbol

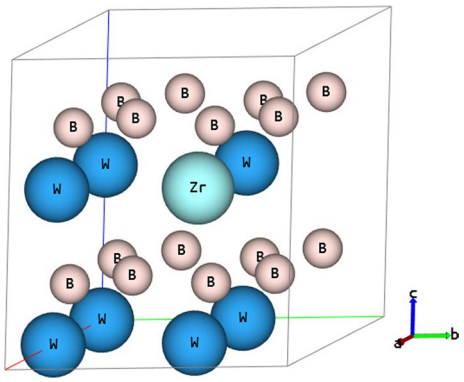

Fig. 23 $W_{0.875}Zr_{0.125}B_2$: basic cell

_atom_site_symmetry_multiplicity
_atom_site_Wyckoff_label
_atom_site_fract_x
_atom_site_fract_y
_atom_site_fract_z
_atom_site_occupancy
B1 B 12 o 0.16803 0.33607 0.24710 1.00000
W1 W 3 f 0.50000 0.00000 0.00000 1.00000
W2 W 3 g 0.50000 0.00000 0.50000 1.00000
B2 B 4 h 0.33333 0.66667 0.24802 1.00000
W3 W 1 a 0.00000 0.00000 0.00000 1.00000
Zr1 Zr 1 b 0.00000 0.00000 0.50000 1.00000

Stiffness tensor:

$$[C_{IJ}] \rightarrow \begin{bmatrix} 541.56 & 200.813 & 111.13 & 0.0 & 0.0 & 0.0 \\ 200.813 & 532.753 & 112.813 & 0.0 & 0.0 & 0.0 \\ 111.13 & 112.813 & 852.923 & 0.0 & 0.0 & 0.0 \\ 0.0 & 0.0 & 0.0 & 231.813 & 0.0 & 0.0 \\ 0.0 & 0.0 & 0.0 & 0.0 & 229.596 & 0.0 \\ 0.0 & 0.0 & 0.0 & 0.0 & 0.0 & 166.8 \end{bmatrix} \text{[GPa]}.$$

_cell_volume 235.932074

loop_
_space_group_symop_id
_space_group_symop_operation_xyz
1 x,y,z
2 x-y,x,z
3 -y,x-y,z
4 -x,-y,z
5 -x+y,-x,z
6 y,-x+y,z
7 x-y,-y,-z
8 x,x-y,-z
9 y,x,-z
10 -x+y,y,-z
11 -x,-x+y,-z
12 -y,-x,-z
13 -x,-y,-z
14 -x+y,-x,-z
15 y,-x+y,-z
16 x,y,-z
17 x-y,x,-z
18 -y,x-y,-z
19 -x+y,y,z
20 -x,-x+y,z
21 -y,-x,z
22 x-y,-y,z
23 x,x-y,z
24 y,x,z

$W_{0.889}Zr_{0.111}B_2$

W8Zr1B18

_symmetry_space_group_name_H-M "P 6/m 2/m 2/m"
_symmetry_Int_Tables_number 191

_cell_length_a 9.04397
_cell_length_b 9.04397
_cell_length_c 3.33072
_cell_angle_alpha 90.00000
_cell_angle_beta 90.00000
_cell_angle_gamma 120.00000

loop_
_atom_site_label
_atom_site_type_symbol
_atom_site_symmetry_multiplicity
_atom_site_Wyckoff_label
_atom_site_fract_x
_atom_site_fract_y
_atom_site_fract_z
_atom_site_occupancy
B1 B 6 m 0.55566 0.11132 0.50000 1.00000
W1 W 6 j 0.33553 0.00000 0.00000 1.00000
B2 B 6 m 0.22302 0.44605 0.50000 1.00000

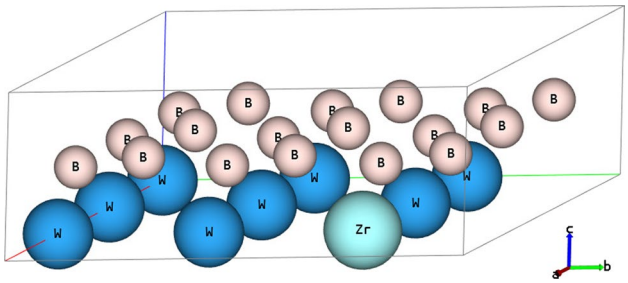

Fig. 24 $W_{0.889}Zr_{0.111}B_2$: basic cell

W2 W 2 c 0.33333 0.66667 0.00000 1.00000
B3 B 6 m 0.11324 0.22648 0.50000 1.00000
Zr1 Zr 1 a 0.00000 0.00000 0.00000 1.00000

Stiffness tensor:

$$[C_{IJ}] \rightarrow \begin{bmatrix} 541.56 & 200.813 & 111.13 & 0.0 & 0.0 & 0.0 \\ 200.813 & 532.753 & 112.813 & 0.0 & 0.0 & 0.0 \\ 111.13 & 112.813 & 852.923 & 0.0 & 0.0 & 0.0 \\ 0.0 & 0.0 & 0.0 & 231.813 & 0.0 & 0.0 \\ 0.0 & 0.0 & 0.0 & 0.0 & 229.596 & 0.0 \\ 0.0 & 0.0 & 0.0 & 0.0 & 0.0 & 166.8 \end{bmatrix} [\text{GPa}].$$

$W_{0.915}Zr_{0.085}B_2$

W11Zr1B24

_symmetry_space_group_name_H-M “P 1 2/m 1”
_symmetry_Int_Tables_number 10

_cell_length_a 6.01639
_cell_length_b 6.64980
_cell_length_c 7.96362
_cell_angle_alpha 90.00000
_cell_angle_beta 100.93409

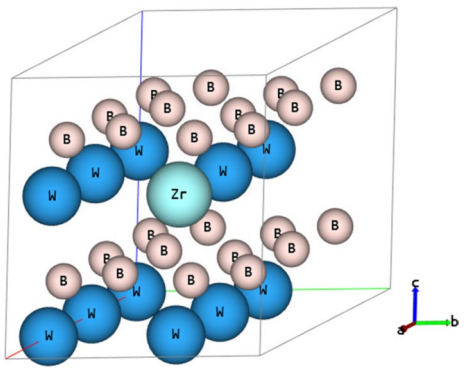

Fig. 25 $W_{0.915}Zr_{0.085}B_2$: basic cell

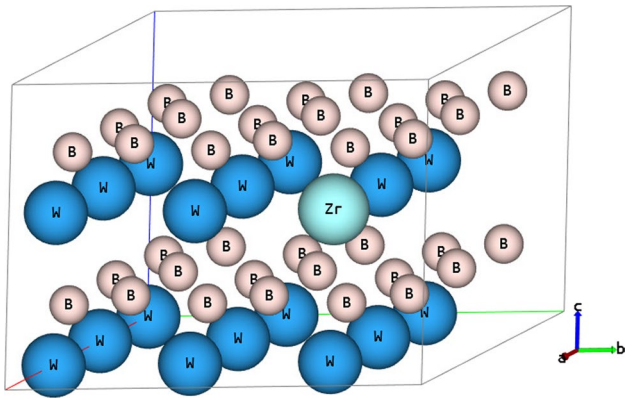

Fig. 26 $W_{0.944}Zr_{0.056}B_2$: basic cell

_cell_angle_gamma 90.00000
_cell_volume 312.822851

loop_
_space_group_symop_id
_space_group_symop_operation_xyz
1 x,y,z
2 -x,y,-z
3 -x,-y,-z
4 x,-y,z

loop_
_atom_site_label
_atom_site_type_symbol
_atom_site_symmetry_multiplicity
_atom_site_Wyckoff_label
_atom_site_fract_x
_atom_site_fract_y
_atom_site_fract_z
_atom_site_occupancy
B1 B 4 o 0.61118 0.74869 -0.05524 1.00000
B2 B 4 o 0.88866 0.75002 0.05511 1.00000
W1 W 2 m 0.83219 0.00000 0.83554 1.00000
W2 W 2 n 0.83280 0.50000 0.83413 1.00000
W3 W 2 m 0.33573 0.00000 0.83609 1.00000

W4 W 2 n 0.33416 0.50000 0.83251 1.00000
B3 B 4 o -0.05606 0.75348 0.27544 1.00000
B4 B 4 o 0.22387 0.75314 0.38764 1.00000
B5 B 4 o 0.44423 0.75158 0.27691 1.00000
B6 B 4 o 0.71982 0.75327 0.38771 1.00000
W5 W 1 g 0.50000 0.00000 0.50000 1.00000
W6 W 1 h 0.50000 0.50000 0.50000 1.00000
W7 W 1 c 0.00000 0.00000 0.50000 1.00000
Zr1 Zr 1 f 0.00000 0.50000 0.50000 1.00000

Stiffness tensor:

$$[C_{IJ}] \rightarrow \begin{bmatrix} 589.155 & 166.568 & 249.71 & 0.0 & 0.0 & 10.949 \\ 166.568 & 612.548 & 251.081 & 0.0 & 0.0 & -11.842 \\ 249.71 & 251.081 & 358.876 & 0.0 & 0.0 & 0.0 \\ 0.0 & 0.0 & 0.0 & 154.191 & -3.577 & 0.0 \\ 0.0 & 0.0 & 0.0 & -3.577 & 151.389 & 0.0 \\ 10.949 & -11.842 & 0.0 & 0.0 & 0.0 & 242.543 \end{bmatrix} \text{[GPa]}.$$

13 -x,-y,-z
14 -x+y,-x,-z
15 y,-x+y,-z
16 x,y,-z
17 x-y,x,-z
18 -y,x-y,-z
19 -x+y,y,z
20 -x,-x+y,z
21 -y,-x,z
22 x-y,-y,z
23 x,x-y,z

$W_{0.944}Zr_{0.056}B_2$

W17Zr1B36

_symmetry_space_group_name_H-M “P 6/m 2/m 2/m”
_symmetry_Int_Tables_number 191

_cell_length_a 9.03216
_cell_length_b 9.03216
_cell_length_c 6.63963
_cell_angle_alpha 90.00000
_cell_angle_beta 90.00000
_cell_angle_gamma 120.00000
_cell_volume 469.091675

loop_
_space_group_symop_id
_space_group_symop_operation_xyz
1 x,y,z
2 x-y,x,z
3 -y,x-y,z
4 -x,-y,z
5 -x+y,-x,z
6 y,-x+y,z
7 x-y,-y,-z
8 x,x-y,-z
9 y,x,-z
10 -x+y,y,-z
11 -x,-x+y,-z
12 -y,-x,-z

24 y,x,z

loop_
_atom_site_label
_atom_site_type_symbol
_atom_site_symmetry_multiplicity
_atom_site_Wyckoff_label
_atom_site_fract_x
_atom_site_fract_y
_atom_site_fract_z
_atom_site_occupancy
B1 B 12 o 0.55562 0.11123 0.25118 1.00000
W1 W 6 j 0.33630 0.00000 0.00000 1.00000
W2 W 6 k 0.33321 0.00000 0.50000 1.00000
B2 B 12 o 0.22266 0.44532 0.24936 1.00000

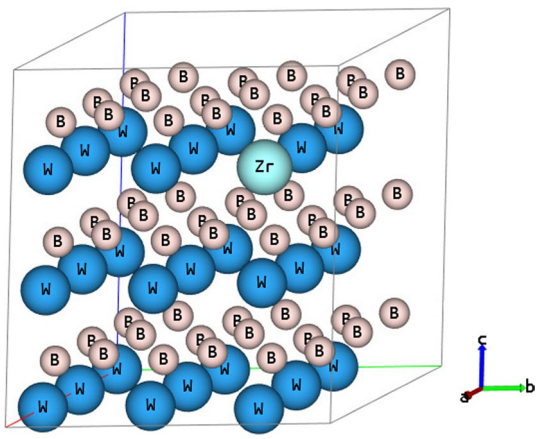

Fig. 27 $W_{0.963}Zr_{0.037}B_2$: basic cell

W3 W 2 c 0.33333 0.66667 0.00000 1.00000
W4 W 2 d 0.33333 0.66667 0.50000 1.00000
B3 B 12 o 0.11229 0.22458 0.24611 1.00000
W5 W 1 a 0.00000 0.00000 0.00000 1.00000
Zr1 Zr 1 b 0.00000 0.00000 0.50000 1.00000

Stiffness tensor:

$$[C_{IJ}] \rightarrow \begin{bmatrix} 579.088 & 146.89 & 247.601 & 0.0 & 0.0 & 0.0 \\ 146.89 & 579.088 & 247.601 & 0.0 & 0.0 & 0.0 \\ 247.601 & 247.601 & 395.545 & 0.0 & 0.0 & 0.0 \\ 0.0 & 0.0 & 0.0 & 140.548 & 0.0 & 0.0 \\ 0.0 & 0.0 & 0.0 & 0.0 & 140.548 & 0.0 \\ 0.0 & 0.0 & 0.0 & 0.0 & 0.0 & 216.099 \end{bmatrix} \text{[GPa]}.$$

4 -x,-y,z
5 -x+y,-x,z
6 y,-x+y,z
7 x-y,-y,-z
8 x,x-y,-z
9 y,x,-z
10 -x+y,y,-z

$W_{0.963}Zr_{0.037}B_2$

W26Zr1B54

_symmetry_space_group_name_H-M “P 6/m 2/m 2/m”
_symmetry_Int_Tables_number 191

_cell_length_a 9.02400
_cell_length_b 9.02400
_cell_length_c 9.96589
_cell_angle_alpha 90.00000
_cell_angle_beta 90.00000
_cell_angle_gamma 120.00000
_cell_volume 702.821288

loop_
_space_group_symop_id
_space_group_symop_operation_xyz
1 x,y,z
2 x-y,x,z
3 -y,x-y,z

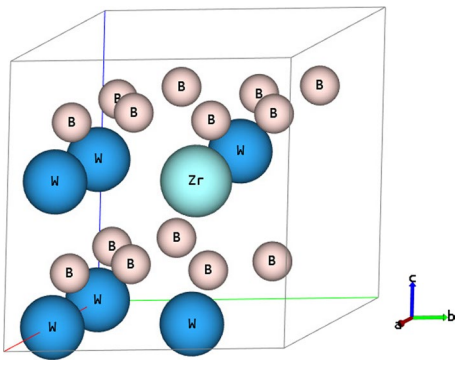

Fig. 28 $W_{0.857}Zr_{0.143}B_2$: basic cell

11 -x,-x+y,-z
12 -y,-x,-z
13 -x,-y,-z
14 -x+y,-x,-z
15 y,-x+y,-z
16 x,y,-z
17 x-y,x,-z
18 -y,x-y,-z
19 -x+y,y,z
20 -x,-x+y,z
21 -y,-x,z
22 x-y,-y,z
23 x,x-y,z
24 y,x,z

loop_
_atom_site_label
_atom_site_type_symbol
_atom_site_symmetry_multiplicity
_atom_site_Wyckoff_label
_atom_site_fract_x
_atom_site_fract_y
_atom_site_fract_z
_atom_site_occupancy
B1 B 6 l 0.55596 0.11193 0.00000 1.00000
W1 W 12 n 0.33451 0.00000 0.83643 1.00000
B2 B 12 o 0.55543 0.11085 0.33286 1.00000
W2 W 6 k 0.33409 0.00000 0.50000 1.00000
B3 B 6 l 0.22219 0.44437 0.00000 1.00000
W3 W 4 h 0.33333 0.66667 0.83149 1.00000
B4 B 12 o 0.22268 0.44535 0.33264 1.00000
W4 W 2 d 0.33333 0.66667 0.50000 1.00000
B5 B 6 l 0.11021 0.22042 0.00000 1.00000
B6 B 12 o 0.11271 0.22542 0.33155 1.00000
W5 W 2 e 0.00000 0.00000 0.82390 1.00000
Zr1 Zr 1 b 0.00000 0.00000 0.50000 1.00000

Stiffness tensor:

$$[\mathbf{C_{IJ}}] \rightarrow \begin{bmatrix} 637.198 & 156.641 & 365.152 & 0.0 & 0.0 & 0.0 \\ 156.641 & 637.198 & 365.152 & 0.0 & 0.0 & 0.0 \\ 365.152 & 365.152 & 621.481 & 0.0 & 0.0 & 0.0 \\ 0.0 & 0.0 & 0.0 & 127.128 & 0.0 & 0.0 \\ 0.0 & 0.0 & 0.0 & 0.0 & 127.128 & 0.0 \\ 0.0 & 0.0 & 0.0 & 0.0 & 0.0 & 240.279 \end{bmatrix} \text{[GPa].}$$

$W_{0.857}Zr_{0.143}B_2$

W6Zr1B14

_symmetry_space_group_name_H-M “P 1”
_symmetry_Int_Tables_number 1

_cell_length_a 6.03601
_cell_length_b 6.04290
_cell_length_c 6.25867
_cell_angle_alpha 89.83236
_cell_angle_beta 89.56667
_cell_angle_gamma 60.69363
_cell_volume 199.062148

loop_
_space_group_symop_id
_space_group_symop_operation_xyz
1 x,y,z

loop_
_atom_site_label
_atom_site_type_symbol
_atom_site_symmetry_multiplicity
_atom_site_Wyckoff_label
_atom_site_fract_x
_atom_site_fract_y
_atom_site_fract_z
_atom_site_occupancy
B1 B 1 a 0.16139 0.67169 0.75807 1.00000
B2 B 1 a 0.33299 0.84362 0.75645 1.00000
W1 W 1 a 0.00361 0.00000 -0.00481 1.00000
B3 B 1 a 0.16192 0.66647 0.23859 1.00000
B4 B 1 a 0.32823 0.83628 0.25006 1.00000
W2 W 1 a 0.00301 0.01037 0.51182 1.00000
B5 B 1 a 0.16283 0.17291 0.24016 1.00000
B6 B 1 a 0.32663 0.33426 0.23828 1.00000
W3 W 1 a -0.00929 0.50837 0.49203 1.00000
B7 B 1 a 0.67666 0.66107 0.75921 1.00000
B8 B 1 a 0.84042 0.82398 0.76028 1.00000
W4 W 1 a 0.50775 -0.00822 0.00262 1.00000
B9 B 1 a 0.66815 0.66670 0.23928 1.00000
B10 B 1 a 0.83509 0.83142 0.24188 1.00000
W5 W 1 a 0.50062 -0.00329 0.50264 1.00000
B11 B 1 a 0.66578 0.16036 0.75734 1.00000
B12 B 1 a 0.83819 0.33106 0.75609 1.00000
W6 W 1 a 0.50253 0.49650 -0.00239 1.00000
B13 B 1 a 0.66758 0.16642 0.24922 1.00000
B14 B 1 a 0.83657 0.33423 0.24085 1.00000
Zr1 Zr 1 a 0.49074 0.49715 0.50745 1.00000

Stiffness tensor:

$$[\mathbf{C_{IJ}}] \rightarrow \begin{bmatrix} 638.182 & 154.256 & 194.818 & 0.0 & 17.390 & -3.647 \\ 154.256 & 616.863 & 195.697 & 4.385 & 0.0 & 0.0 \\ 194.818 & 195.697 & 505.912 & 5.658 & 15.659 & 3.581 \\ 0.0 & 4.385 & 5.658 & 236.073 & 2.019 & 4.817 \\ 17.390 & 0.0 & 15.659 & 2.019 & 233.391 & 5.405 \\ -3.647 & 0.0 & 3.581 & 4.817 & 5.405 & 241.134 \end{bmatrix} \text{[GPa].}$$

Acknowledgements Additional support for the work was provided by the computing cluster GRAFEN at Biocentrum Ochota, the Interdisciplinary Centre for Mathematical and Computational Modelling of Warsaw University (ICM UW) and Poznań Supercomputing and Networking Center (PSNC).

Funding This study was funded by the National Science Centre (NCN – Poland) Research Project: UMO-2017/25/B/ST8/01789 and project SUPERCOAT; project number: TECHMASTRATEG-III/0017/2019.

Declarations

Conflict of interest The authors declare that they have no conflict of interest.

Ethical approval This article does not contain any studies with human participants or animals performed by any of the authors.

References

1. Yeung MT, Mohammadi R, Kaner RB. Ultraincompressible, superhard materials. Annu Rev Mater Res. 2016;46(1):465–85. https://doi.org/10.1146/annurev-matsci-070115-032148.
2. Debnárová S, Souček P, Vašina P, Zábranský L, Buršíková V, Mirzaei S, Pei YT. The tribological properties of short range ordered W-B-C protective coatings prepared by pulsed magnetron sputtering. Surf Coat Technol. 2019;357:364–71. https://doi.org/10.1016/j.surfcoat.2018.10.026.
3. Windsor CG, Astbury JO, Morgan JG, Wilson CL, Humphry-Baker SA. Activation and transmutation of tungsten boride shields in a spherical tokamak. Nucl Fusion. 2022;62(3): 036009. https://doi.org/10.1088/1741-4326/ac4866.
4. Akopov G, Yeung MT, Kaner RB. Rediscovering the crystal chemistry of borides. Adv Mater. 2017;29(21):1604506. https://doi.org/10.1002/adma.201604506.
5. Fuger C, Moraes V, Hahn R, Bolvardi H, Polcik P, Riedl H, Mayrhofer PH. Influence of Tantalum on phase stability and mechanical properties of WB_2. MRS Commun. 2019;9(1):375–80. https://doi.org/10.1557/mrc.2019.5.
6. Psiuk R, Milczarek M, Jenczyk P, Denis P, Jarząbek DM, Bazarnik P, Pisarek M, Mościcki T. Improved mechanical properties of W-Zr-B coatings deposited by hybrid RF magnetron-PLD method. Appl Surf Sci. 2021;570: 151239. https://doi.org/10.1016/j.apsusc.2021.151239.
7. Mościcki T, Psiuk R, Radziejewska J, Wiśniewska M, Garbiec D. Properties of spark plasma sintered compacts and magnetron sputtered coatings made from Cr, Mo, Re and Zr alloyed tungsten diboride. Coatings. 2021;11:11.
8. Fuger C, Schwartz B, Wojcik T, Moraes V, Weiss M, Limbeck A, Macauley CA, Hunold O, Polcik P, Primetzhofer D, Felfer P, Mayrhofer PH, Riedl H. Influence of Ta on the oxidation resistance of WB_{2-z} coatings. J Alloy Compd. 2021;864: 158121. https://doi.org/10.1016/j.jallcom.2020.158121.
9. Mościcki T, Chrzanowska-Giżyńska J, Psiuk R, Denis P, Mulewska K, Kurpaska L, Chmielewski M, Wiśniewska M, Garbiec D. Thermal and mechanical properties of (W, Zr)B_{2-z} coatings deposited by RF magnetron sputtering method. Int J Refract Metal Hard Mater. 2022;105: 105811. https://doi.org/10.1016/j.ijrmhm.2022.105811.
10. Moraes V, Riedl H, Fuger C, Polcik P, Bolvardi H, Holec D, Mayrhofer PH. Ab initio inspired design of ternary boride thin films. Sci Rep. 2018;8:9288. https://doi.org/10.1038/s41598-018-27426-w.
11. Cheng X-Y, Chen X-Q, Li D-Z, Li Y-Y. Computational materials discovery: the case of the W-B system. Acta Crystallogr C. 2014;70(2):85–103. https://doi.org/10.1107/S2053229613027551.
12. Euchner H, Mayrhofer PH, Riedl H, Klimashin FF, Limbeck A, Polcik P, Kolozsvari S. Solid solution hardening of vacancy stabilized $Ti_xW_{1-x}B_2$. Acta Mater. 2015;101:55–61. https://doi.org/10.1016/j.actamat.2015.08.048.
13. Maździarz M, Mościcki T. Structural, mechanical and optical properties of potentially superhard WB_x polymorphs from first principles calculations. Mater Chem Phys. 2016;179:92–102. https://doi.org/10.1016/j.matchemphys.2016.05.014.
14. Fuger C, Hahn R, Zauner L, Wojcik T, Weiss M, Limbeck A, Hunold O, Polcik P, Riedl H. Anisotropic super-hardness of hexagonal WB2 ±z thin films. Mater Res Lett. 2022;10(2):70–7. https://doi.org/10.1080/21663831.2021.2021308.
15. Chang YA, Pike LM, Liu CT, Bilbrey AR, Stone DS. Correlation of the hardness and vacancy concentration in FeAl. Intermetallics. 1993;1(2):107–15. https://doi.org/10.1016/0966-9795(93)90028-T.
16. Zhu X, Gao X, Song H, Han G, Lin D-Y. Effects of vacancies on the mechanical properties of zirconium: an ab initio investigation. Mater Des. 2017;119:30–7. https://doi.org/10.1016/j.matdes.2017.01.060.
17. Pan Y, Chen S, Lin Y. Vacancy-induced elastic properties and hardness of CrB_4: A DFT calculation. Int J Mod Phys B. 2017;31(13):1750096. https://doi.org/10.1142/S0217979217500965.
18. Gu X, Liu C, Guo H, Zhang K, Chen C. Sorting transition-metal diborides: new descriptor for mechanical properties. Acta Mater. 2021;207: 116685. https://doi.org/10.1016/j.actamat.2021.116685.
19. Maździarz M, Mościcki T. New zirconium diboride polymorphs—first-principles calculations. Materials. 2020;13:13. https://doi.org/10.3390/ma13133022.
20. Hohenberg P, Kohn W. Inhomogeneous electron gas. Phys Rev. 1964;136:864–71. https://doi.org/10.1103/PhysRev.136.B864.
21. Kohn W, Sham LJ. Self-consistent equations including exchange and correlation effects. Phys Rev. 1965;140:1133–8. https://doi.org/10.1103/PhysRev.140.A1133.
22. Gonze X, Jollet F, Araujo FA, Adams D, Amadon B, Applencourt T, Audouze C, Beuken J-M, Bieder J, Bokhanchuk A, Bousquet E, Bruneval F, Caliste D, Côté M, Dahm F, Pieve FD, Delaveau M, Gennaro MD, Dorado B, Espejo C, Geneste G, Genovese L, Gerossier A, Giantomassi M, Gillet Y, Hamann

DR, He L, Jomard G, Janssen JL, Roux SL, Levitt A, Lherbier A, Liu F, Lukačević I, Martin A, Martins C, Oliveira MJT, Poncé S, Pouillon Y, Rangel T, Rignanese G-M, Romero AH, Rousseau B, Rubel O, Shukri AA, Stankovski M, Torrent M, Setten MJV, Troeye BV, Verstraete MJ, Waroquiers D, Wiktor J, Xu B, Zhou A, Zwanziger JW. Recent developments in the ABINIT software package. Comput Phys Commun. 2016;205:106–31. https://doi.org/10.1016/j.cpc.2016.04.003.

23. ...Gonze X, Amadon B, Antonius G, Arnardi F, Baguet L, Beuken J-M, Bieder J, Bottin F, Bouchet J, Bousquet E, Brouwer N, Bruneval F, Brunin G, Cavignac T, Charraud J-B, Chen W, Côté M, Cottenier S, Denier J, Geneste G, Ghosez P, Giantomassi M, Gillet Y, Gingras O, Hamann DR, Hautier G, He X, Helbig N, Holzwarth N, Jia Y, Jollet F, Lafargue-Dit-Hauret W, Lejaeghere K, Marques MAL, Martin A, Martins C, Miranda HPC, Naccarato F, Persson K, Petretto G, Planes V, Pouillon Y, Prokhorenko S, Ricci F, Rignanese G-M, Romero AH, Schmitt MM, Torrent M, van Setten MJ, Troeye BV, Verstraete MJ, Zérah G, Zwanziger JW. The ABINIT project: impact, environment and recent developments. Comput Phys Commun. 2020;248: 107042. https://doi.org/10.1016/j.cpc.2019.107042.
24. Martin A, Torrent M, Caracas R. Projector augmented-wave formulation of response to strain and electric-field perturbation within density functional perturbation theory. Phys Rev B. 2019;99: 094112. https://doi.org/10.1103/PhysRevB.99.094112.
25. Zhao E, Meng J, Ma Y, Wu Z. Phase stability and mechanical properties of tungsten borides from first principles calculations. Phys Chem Chem Phys. 2010;12:13158–65. https://doi.org/10.1039/C004122J.
26. Bloch F. Bemerkung zur Elektronentheorie des Ferromagnetismus und der elektrischen Leitfähigkeit. Z Phys. 1929;57:545–55. https://doi.org/10.1007/BF01340281.
27. Perdew JP, Wang Y. Accurate and simple analytic representation of the electron-gas correlation energy. Phys Rev B. 1992;45:13244–9. https://doi.org/10.1103/PhysRevB.45.13244.
28. Jollet F, Torrent M, Holzwarth N. Generation of projector augmented-wave atomic data: a 71 element validated table in the XML format. Comput Phys Commun. 2014;185(4):1246–54. https://doi.org/10.1016/j.cpc.2013.12.023.
29. Qi C, Jiang Y, Liu Y, Zhou R. Elastic and electronic properties of XB_2 (X=V, Nb, Ta, Cr, Mo, and W) with AlB_2 structure from first principles calculations. Ceram Int. 2014;40(4):5843–51. https://doi.org/10.1016/j.ceramint.2013.11.026.
30. Maździarz M, Mościcki T. Structural, mechanical, optical, thermodynamical and phonon properties of stable ReB_2 polymorphs from density functional calculations. J Alloy Compd. 2016;657:878–88. https://doi.org/10.1016/j.jallcom.2015.10.133.
31. Hamann DR, Wu X, Rabe KM, Vanderbilt D. Metric tensor formulation of strain in density-functional perturbation theory. Phys Rev B. 2005;71: 035117. https://doi.org/10.1103/PhysRevB.71.035117.
32. Hill R. The elastic behaviour of a crystalline aggregate. Proc Phys Soc Sect A. 1952;65(5):349–54. https://doi.org/10.1088/0370-1298/65/5/307.
33. Maździarz M, Gajewski M. Estimation of isotropic hyperelasticity constitutive models to approximate the atomistic simulation data for aluminium and tungsten monocrystals. Comput Model Eng Sci. 2015;105(2):123–50. https://doi.org/10.3970/cmes.2015.105.123.
34. Grimvall G, Magyari-Köpe B, Ozoliņš V, Persson KA. Lattice instabilities in metallic elements. Rev Mod Phys. 2012;84:945–86. https://doi.org/10.1103/RevModPhys.84.945.
35. Maździarz M. Comment on 'The Computational 2D Materials Database: high-throughput modeling and discovery of atomically thin crystals'. 2D Mater. 2019;6(4): 048001. https://doi.org/10.1088/2053-1583/ab2ef3.
36. Mazhnik E, Oganov AR. Application of machine learning methods for predicting new superhard materials. J Appl Phys. 2020;128(7): 075102. https://doi.org/10.1063/5.0012055.
37. Pugh SFXCII. Relations between the elastic moduli and the plastic properties of polycrystalline pure metals. Lond Edinburgh Dublin Philos Mag J Sci. 1954;45(367):823–43. https://doi.org/10.1080/14786440808520496.
38. Musil J. Flexible hard nanocomposite coatings. RSC Adv. 2015;5:60482–95. https://doi.org/10.1039/C5RA09586G.
39. Garbiec D, Wiśniewska M, Psiuk R, Denis P, Levintant-Zayonts N, Leshchynsky V, Rubach R, Mościcki T. Zirconium alloyed tungsten borides synthesized by spark plasma sintering. Arch Civ Mech Eng. 2021;21(1):37. https://doi.org/10.1007/s43452-021-00188-5.
40. Laugier MT. New formula for indentation toughness in ceramics. J Mater Sci Lett. 1987;6(3):355–6. https://doi.org/10.1007/BF01729352.
41. Smolik J, Kacprzyńska-Gołacka J, Sowa S, Piasek A. The analysis of resistance to brittle cracking of tungsten doped TiB2 coatings obtained by magnetron sputtering. Coatings. 2020;10:9. https://doi.org/10.3390/coatings10090807.
42. Euchner H, Mayrhofer PH. Designing thin film materials—ternary borides from first principles. Thin Solid Films. 2015;583:46–9. https://doi.org/10.1016/j.tsf.2015.03.035.
43. Nye J. Physical properties of crystals: their representation by tensors and matrices. United Kingdom: Oxford University Press; 1957.
44. Kroker M, Souček P, Šlapanská M, Sochora V, Jílek M, Vašina P. Predicting the composition of W-B-C coatings sputtered from industrial cylindrical segmented target. Surf Coat Technol. 2022;438: 128411. https://doi.org/10.1016/j.surfcoat.2022.128411.
45. Mościcki T, Psiuk R, Słomińska H, Levintant-Zayonts N, Garbiec D, Pisarek M, Bazarnik P, Nosewicz S, Chrzanowska-Giżyńska J. Influence of overstoichiometric boron and titanium addition on the properties of rf magnetron sputtered tungsten borides. Surf Coat Technol. 2020;390: 125689. https://doi.org/10.1016/j.surfcoat.2020.125689.
46. Bakhit B, Palisaitis J, Wu Z, Sortica MA, Primetzhofer D, Persson K, Rosen J, Hultman L, Petrov I, Greene JE, Greczynski G. Age hardening in superhard ZrB_2-rich $Zr_{1-x}Ta_xB_y$ thin films. Scripta Mater. 2021;191:120–5. https://doi.org/10.1016/j.scriptamat.2020.09.026.
47. Wagner A, Holec D, Mayrhofer PH, Bartosik M. Enhanced fracture toughness in ceramic superlattice thin films: On the role of coherency stresses and misfit dislocations. Mater Des. 2021;202: 109517. https://doi.org/10.1016/j.matdes.2021.109517.
48. Ordan'yan SS, Boldin AA, Suvorov SS, Smirnov VV. Phase diagram of the W_2B_5-ZrB_2 system. Inorg Mater. 2005;41(3):232–4. https://doi.org/10.1007/s10789-005-0114-0.
49. Thornton JA. Influence of apparatus geometry and deposition conditions on the structure and topography of thick sputtered coatings. J Vac Sci Technol. 1974;11(4):666–70. https://doi.org/10.1116/1.1312732.
50. Moraes V, Fuger C, Paneta V, Primetzhofer D, Polcik P, Bolvardi H, Arndt M, Riedl H, Mayrhofer PH. Substoichiometry and tantalum dependent thermal stability of α-structured W-Ta-B thin films. Scripta Mater. 2018;155:5–10. https://doi.org/10.1016/j.scriptamat.2018.06.005.

51. Powder Diffraction File 04-007-1000, International Center for Diffraction Data2011
52. Powder Diffraction File 000-34-0423 International Center for Diffraction Data2011
53. Powder Diffraction File 04-003-6624, International Center for Diffraction Data2011
54. Barna PB, Adamik M. Fundamental structure forming phenomena of polycrystalline films and the structure zone models. Thin Solid Films. 1998;317(1):27–33. https://doi.org/10.1016/S0040-6090(97)00503-8.
55. Mayrhofer PH, Mitterer C, Wen JG, Greene JE, Petrov I. Self-organized nanocolumnar structure in superhard TiB_2 thin films. Appl Phys Lett. 2005;86(13): 131909. https://doi.org/10.1063/1.1887824.
56. Bakhit B, Engberg DLJ, Lu J, Rosen J, Högberg H, Hultman L, Petrov I, Greene JE, Greczynski G. Strategy for simultaneously increasing both hardness and toughness in ZrB_2-rich $Zr_{1-x}Ta_xB_y$ thin films. J Vacuum Sci Technol A. 2019;37(3): 031506. https://doi.org/10.1116/1.5093170.